University of Alberta

Fabrication, characterization and application of functional coatings on nickel foam to resist hydrogen sulfide corrosion and metal dusting at high temperature

by

Qing Xun Low

A thesis submitted to the Faculty of Graduate Studies and Research
in partial fulfillment of the requirements for the degree of

Master of Science
in
Chemical Engineering

Chemical and Material Engineering

Fall 2011
Edmonton, Alberta

Abstract

Electrodeposition and co-electrodeposition methods were used to prepare: (1) copper coated nickel foam; (2) copper-ceria coated nickel foam. Both of these coatings formed a copper-nickel alloy after heat treatment in reducing atmosphere. These coatings have low, stable resistance when exposed to 500 ppm H_2S-syngas at 750 ^oC. The copper-ceria coated nickel foam showed better resistance to H_2S corrosion compared to copper coated nickel foam. This was because ceria acted as sulfur adsorbent which reduced the sulfidation rate. However, for the copper-ceria coating, cracks were formed and dense layer of coating could not be obtained thus making it unsuitable for use as an anode current collector in SOFCs applications. In contrast, for uncoated nickel foams exposed to either syngas or 500 ppm H_2S-syngas, the bare nickel was severely cracked, causing loss of mechanical strength and large increase in resistance.

Electrophoretic deposition was used as the coating technique for the ceramic coating. This coating is used to resist H_2S corrosion for H_2S level up to 5000 ppm. Titanium oxide was first used as the coating material since it can be commercially obtained and was used to help understand the process. The optimum suspension used for deposition contained 2 wt% titanium oxide, 2 wt% triethanolamine (TEA) and 1 wt% poly(vinyl butral-co-vinyl) (PVB). Cracks-free coating can be obtained after deposition. However, cracks were present when the titanium oxide coated samples were heated at high temperature.

Acknowledgement

I am deeply grateful to Dr. Jingli Luo for her supervision and guidance throughout this study. I also want to thank Dr. Xian-Zhu Fu who always devotes his invaluable time to discuss and help me in this research.

The funding for this research work was provided by Natural Science and Engineering Research Council of Canada (NSERC) as well as Vale Inc. I would also thank the comments and advices provided by Drs. Alan Sanger, Juri Melnik, and Quan Yang.

Above all, I am especially thankful for my parents who encourage me to continue with my studies to higher levels. I also want to thank my girl friend Weishan Huang, who has made my life the happiest ever. Without her encouragement and inspiration, I would not be able to accomplish my thesis.

Table of contents

List of Tables

List of Figures

List of symbols

M	atomic weight
a_c	Carbon activity
I	current
^oC	degree Celsius
ε	dielectric constant
ρ	density
K	equilibrium constant
μ	electrophoretic mobility
F	Faraday constant, 96485 C/mol
R	resistance
t	time
η	viscosity
ζ	zeta potential

List of abbreviations

AFC	alkaline fuel cells
CHP	co-production of heat and power
CTE	Coefficient of thermal expansion
EDS	energy dispersive X-ray
EPD	electrophoretic deposition
MCFC	molten carbonate fuel cells
PAFC	phosphoric acid fuel cells
PEMFC	polymer electrolyte fuel cells
ppm	Part per million
PSD	Particles size distribution
PVB	poly(vinyl butral-co-vinyl)
SEM	Scanning electron microscope
SOFC	solid oxide fuel cells
TEA	triethanolamine
wt%	Weight percent
XRD	X-ray diffraction

1.0 Solid oxide fuel cells

1.1. Introduction

Our present society is largely dependent on fossil fuels for energy. However, there is growing concern that using fossil fuels causes environmental pollution. Furthermore, our reliance and usage of fossil fuel are increasing, leading to the depletion of the known natural fossil fuel resources. Renewable energies are one potential solution to these problems and efforts have been made for finding and developing renewable energy [1, 2]. Renewable energies, including solar power, wind power, wave power, and geothermal power, are often large scale projects and their applications are limited by natural and geographical limitations. In parallel, fuel cells have attracted intense interest as efficient, clean and flexible means for electricity generation because they can be scaled up for large, stationary power generation and scaled down for mobile and portable applications.

1.2. Solid oxide fuel cell operation

Fuel cells are electrochemical devices that transform chemical energy available from conversion of a fuel and an oxidant into electricity [3]. The fuel and oxidant are supplied from external sources into separate fuel cell compartments separated by an ion conducting medium. Fuel cells have similar operating principles to primary batteries, except that they can continue to generate electricity as long as the fuel and oxidant are supplied continually. Different types of fuel cells have been developed for various applications. Based on the nature of the electrolyte used, fuel cells are categorized into alkaline fuel cells (AFC), phosphoric acid fuel cells (PAFC), molten carbonate fuel cells (MCFC), solid

oxide fuel cells (SOFC) and polymer electrolyte fuel cells (PEMFC). The topic of the present report is development of materials and their applications in SOFC.

The basic components of SOFC are two electrodes (anode and cathode), a ceramic membrane electrolyte and interconnects (Fig. 1.1). The electrolyte is sandwiched between the electrodes. At the anode side, fuel is oxidized by oxygen ions conducted through the electrolyte to form water and release electrons. An external circuit is used to connect the load, cathode and anode (Fig. 1.2). The electrons released at the anode electrode flow through the anode current collector to the external circuit, across the load to do work, then through the cathode current collector to the porous cathode. At the cathode, the oxygen reacts with the incoming electrons and form oxide ions. The oxide ions migrate as an ion current through the electrolyte to react with the fuel in anode. Typically, commercialized SOFC has an operating temperature in the range of 900-1000 ^{o}C. Many researches has been conducted to decrease the operating temperature of SOFCs to 600-800 ^{o}C. The high (i.e. 900-1000 ^{o}C) to medium operating temperatures (600-800 ^{o}C) provide many advantages and also disadvantages which will be discussed in Section 1.3.

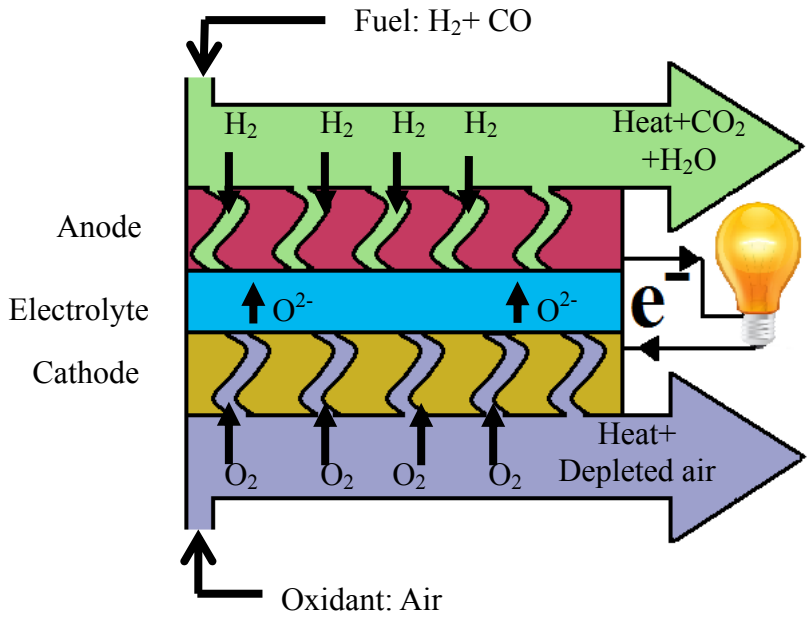

Anode :	Main oxidation reaction:	$2H_2(g)+2O^{2-} \rightarrow 2H_2O(g)+4e^-$
	Water shift reaction:	$CO(g)+H_2O(g) \rightarrow CO_2(g)+H_2(g)$
Cathode:		$O_2(g)+4e^- \rightarrow 2O^{2-}$
Reaction:		$2H_2(g) + O_2(g) \rightarrow 2H_2O(g)$

Figure 1.1. Basic schematic of one design of SOFC.

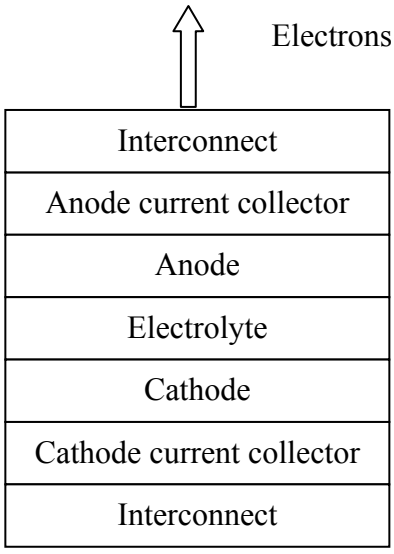

Figure 1.2. The sequence of components in SOFC.

1.3. Advantages and disadvantages of solid oxide fuel cells

SOFCs are capable of operation at high efficiency with respect to fuel utilization. In contrast to traditional electricity generators the efficiency of SOFC is not limited by the Carnot thermodynamic cycle. In moving vehicles fuel cells can achieve efficiencies of 40-50% compared to 20-35% for internal combustion engines [4]. The high grade heat produced by SOFCs can be utilized in standing engine systems for the co-production of heat and power (CHP) which further increases the potential efficiency of conversion of the fuel's chemical energy to 85-90% [1, 5].

The by-products from the electrochemical reaction of SOFCs are water and heat when purified hydrogen is used as fuel. When hydrocarbons such as methane or syngas are used as fuel, carbon dioxide is also produced. Because SOFCs have high efficiency the CO_2 emissions per unit of electricity produced are minimized. In addition, when compared to traditional electricity generators the emissions of nitrogen oxides (i.e.NO_x) and sulfur oxides (i.e.SO_x) are negligible.

SOFCs operate at very high temperature (i.e.900-1000^oC) and this makes them relatively insensitive to the effects of impurities present in most hydrocarbons. In particular, SOFCs are more tolerant of most sulfur contaminants in the feed when compared to other fuel cell systems [6]. SOFCs can utilize a variety of hydrocarbons and related feeds, including syngas, methane, coal gas, gasoline, diesel fuel, etc. These hydrocarbons are much cheaper than purified hydrogen, and they can be stored and transported much more easily.

Fuel cells systems have many advantages, however commercialization of

SOFCs remains a great challenge due to the high costs of material fabrication. In this respect, a disadvantage of SOFC is the high operating temperature (i.e. 900-1000^{o}C). Advanced fabrication techniques and construction materials are needed to withstand the high operating temperature.

The interconnects/current collectors are important components of a fuel cell system. The material used to fabricate interconnects/current collectors must be extremely stable because it is exposed to the oxidizing and reducing side of the cell at high temperature. Moreover, it must be able to conduct electricity which further limits the material selection for interconnect fabrication. Other problems arise when syngas (i.e.a mixture of carbon monoxide, hydrogen and lesser amounts of impurities such as hydrogen sulfide) is used as fuel. These problems include metal dusting and hydrogen sulfide corrosion. Thus modifications are needed for construction of the anode current collector in order to use H_2S-containing syngas.

1.4. SOFC Interconnects/current collectors

The role of interconnects/current collectors is to carry electrical current from the electrochemical cell to the external circuit. The current collectors are a part of interconnects in direct contact with the respective anode and cathode. The contact surface between the current collectors and the corresponding anode and cathode must be large. In addition, the current collectors must be porous to enable facile diffusion of fuel, oxidant and the corresponding redox products. Materials for interconnects/current collectors also must have good electronic conductivity to avoid parasitic losses from overcoming high ohmic resistance. An especially

challenging requirement for interconnects is exposure to oxidizing and reducing atmospheres. The cathode current collector must be stable in the oxidizing atmosphere. The anode current collectors must stable in the reducing atmosphere. Further requirements apply when a hydrocarbon such as methane or syngas is used as fuel. The anode current collectors must resist both carbon deposition and hydrogen sulfide corrosion. The following list summarizes the important requirements for an effective and economically viable anode current collector [7, 8]:

1. Good electrical and thermal conductivity
2. Good stability under multiple fuel gas atmospheres
3. Good resistance to sulfur corrosion and carbon deposition
4. Similar coefficient thermal expansion (CTE) to the anode which prevent the crack between current collector and anode.
5. Low material and fabrication costs

1.4.1. Ceramic interconnects/current collectors

Ceramic current collectors are oxides and are stable in the oxidizing atmosphere at the SOFC cathode [9]. These current collectors have perovskite type structures. Doped lanthanum chromate ($LaCrO_3$) is the most commonly used oxide used for interconnects/current collectors. Dopants used to increase the conductivity include calcium and strontium ions [7, 10-12]. However, the conductivity of these ceramics decreases with decreasing in oxygen partial pressure [10-13]. The drop of electrical conductivity with decreasing oxygen partial pressure is a reflection of reduced electron hole concentration.

Although ceramic interconnects/current collectors provide electronic conductivity, chemical stability in oxidizing atmosphere and similar thermal expansion coefficient to that of the ceramic electrolyte, they are not used widely in SOFCs due to numerous drawbacks. The ceramic is very costly and it is difficult to fabricate into compact and complex shapes [14, 15]. Many of the ceramics used contain chromium ions (Cr^{3+}) which can be oxidized to a Cr^{6+}-containing species (CrO_3 or $CrO_2(OH)_2$) which is volatile. These species diffuse and deposit on the cathode thus degrading fuel cell performance [3].

1.4.2. Metallic interconnects/current collectors

Recently, metallic interconnects/current collectors have been considered as potential substitutes for ceramic interconnects/current collectors. When compared to ceramic materials, metallic materials are easier to form into the required shapes, cheaper, and have high thermal and electronic conductivity, and no ionic conductivity [17-19]. One of the disadvantages of metallic materials is that they have higher thermal expansion coefficient compare to ceramic cell of SOFC [16]. Metallic materials are suitable only for use at low operating temperatures, 600-800^{o}C, due to their lower melting point and, in some cases, high volatility at higher fuel cell operating temperatures [9]. An oxide protective layer usually is formed at high temperature which decreases the conductivity across the interface between the metal and other components. Cracks may form in the protective layer during long term operation [9].

Yang and Stevenson [8] divided the relevant metallic alloys into five groups: Cr-based alloys, ferritic stainless steels, austenitic stainless steels, Fe-Ni-Cr based

super alloys, and nickel based super alloys (Table 1.1). These alloys contain "active" elements such as Cr and Al which can be oxidized and form a protective layer to minimize further environmental attacks [17, 18]. The formation of a non-conductive aluminum oxide (Al_2O_3) layer is detrimental to its use as SOFC interconnects [19]; Semi-conductive chromia (Cr_2O_3) layers have electrical conductivity of 10^{-2} Scm^{-1} at 800 ^oC [20, 21]. However, as the alloys contain chromium ions they can cause chromium poisoning in SOFCs and decrease the cell performance [22].

The Cr-based alloys and ferritic stainless steels are more preferable than the other alloys because of their similar coefficients of thermal expansion compared with those of the other ceramic cell components ($10.5\text{-}12.5x10^{-6}$ K^{-1}) [23]. The austenitic stainless steels, Fe-Ni-Cr based super alloys and Ni-(Fe)-Cr super alloys provide better oxidation resistance than ferritic stainless steels [27-30]. Although such alloys with sufficient Cr content exhibit high oxidation resistance they also have high CTE, which leads to separation between layers, with a consequent increase in resistance and decrease in the fuel cell performance during thermal cycling tests [9].

Table 1.1. Key properties of different alloy groups for SOFC applications [29].

Alloy	CTE* ($10^{-6}K^{-1}$) (RT-800^{o}C)	Oxidation resistance	Fabrication ability	Cost
Cr-based alloys	11-12.5	Good	Difficult	$$
Ferritic stainless steels	11.5-14	Good	Fairly readily	$
Austenitic stainless steels	18-20	Good	Readily	$
Fe-Ni-Cr based super alloys	15-20	Good	Readily	$$$
Ni-(Fe)-Cr super alloys	14-19	Good	Readily	$$

*Coefficient of thermal expansion (CTE); Less Expensive: $; Expensive: $$; Fairly expensive: $$$;

Descriptions of commercialized alloys emphasize the stability of the structure and nature of the protective layer formed in corrosive environments but not their electrical conductivity. The protective layer formed during the process has low or essentially no conductivity. Quadakkers et al. [24] developed Crofer 22 APU alloy (a ferritic stainless steel) which forms a $(Mn,Cr)_3O_4$ spinel upper layer and Cr_2O_3 sublayer and has electrical conductivity double that of Cr_2O_3 [25]. The differences between Crofer 22 APU alloy and ferritic stainless steel is that Crofer

22 APU alloy forms $(Mn,Cr)_3O_4$ spinel upper layer and this layer helps to lower volatility of Cr from the material [26]. However, in the early stages of oxidation chromium is not covered by the spinel layer and the consequent chromium poisoning degrades the performance of fuel cell [27, 28].

Table 1.2. Composition of Crofer 22 APU alloy [26].

Wt%	Fe	Cr	Mn	Si	C	Ti	P	S	La
Crofer 22 APU	Bal	22.8	0.45	0	0.005	0.08	0.016	0.002	0.06

1.4.3. Metallic interconnects/current collectors for anode side

The ceramic and metallic interconnects/current collectors discussed above are commonly used at the cathode side of SOFCs, and these materials also can be used at the anode side if purified hydrogen is used as the fuel. However, the anode environment becomes more complex when hydrocarbons or related fuels are used. The effect of high water vapor pressure, carbon bearing gases and impurities (e.g.hydrogen sulfide) makes metallic interconnects susceptible to various corrosion processes.

In moist hydrogen, a different oxidation behavior was observed for Ni-(Fe)-Cr and Fe-Cr alloys. The formation of nickel oxide is suppressed since the oxidation of nickel is thermodynamically unfavorable in low oxygen activity (in the presence of hydrogen). Thus Ni-(Fe)-Cr base alloys with low Cr content are promising materials for use as interconnects, in terms of oxidation resistance [30, 31]. With Fe-Cr base alloys, the high water vapor content leads to oxidation of Cr and formation of a Cr_2O_3 protective layer, but the layer is prone to break

away when Fe_2O_3 and $(Fe,Cr)_3O_4$ also are formed [32-34]. The potential occurrence of breakaway oxidation is due to the depletion of the Cr reservoir in Fe–Cr alloys.

When a hydrocarbon is used as the fuel, Cr-based alloys, Fe-(Ni)-Cr alloys, Ni-Fe alloys, Ni-Fe-Cr alloys, austenitic stainless steels, Alloy 800, Inconel 601, Inconel 690, and Inconel 693 (the composition of these alloys are shown in Table 1.3) suffer rapid metal dusting [14]. Metal dusting is corrosion degradation of metals and the alloys at high temperatures in a strongly carburizing gas atmosphere. These metals/alloys include low and high alloy steel and Fe-, Ni- and Co-based alloys. Metal dusting corrodes the materials by disintegration into metal powder and graphitic carbon. The degradation of the alloys is caused by disintegration of the metal matrix into very small particles [35]. The resistance of metal alloys to dusting depends on the alloy composition. In this respect, the best alloy is Inconel 625 (protected by chromia) and alumina forming alloys [14]. Zeng and Natesan [36] examined a series of alloys in carbonaceous gases and concluded that: (1) pits were formed on the alloy surface which grew to large holes and disintegration of the alloy into a powder mixture of carbon, carbide and fine particles of metal occurred ; (2) chromia prevents metal dusting, but metal dusting can occur if the alloy major phase is a spinel; (3) nickel-based alloys are much more resistant to metal dusting than iron-based alloys because nickel-based alloys form less spinel; (4) the metal dusting rate increases with an increase in operating pressure.

1.5. Chromia volatility and cell poisoning

A conductive chromia (Cr_2O_3) protective layer is formed on chromia-forming alloys during oxidation in the cathode (by air) and anode (by H_2O-H_2). However, Cr_2O_3 continues to react with O_2 and forms volatile CrO_3 (at temperature > 600 ^oC) [22]:

$$Cr_2O_3(s) + 1.5O_2(g) \rightarrow 2CrO_3(g) \quad (1.1)$$

In the presence of water vapor in anode side, the reaction of Cr_2O_3 and water is [37]:

$$0.5Cr_2O_3(s) + 0.5O_2(g) + H_2O(g) \rightarrow CrO_2(OH)_2(g) \quad (1.2)$$

This chromia-vapor species (i.e. CrO_3 and $CrO_2(OH)_2$) migrates to the cathode and deposit on the cathode and cathode/electrolyte interface, thus degrading the fuel cell performance. For example, the chromia species from Inconel 600 and Fe-Cr base alloy were found to deposit and block the active sites at the triple phase boundary of LSM/YSZ.

Table 1.3. The composition of different alloys.

Alloy	C	Cr	Fe	Ni	Al	Ti	Si	S	Co	Mn	Cu	Nb
800	.06-.10	19-23	39.5	30-35	0.15-0.60	0.15-0.60	-	-	-	-	-	-
Inconnel 601	0.10	21-25	Balance	58-63	1-1.7	-	0.5	0.015	1	1	-	-
Inconnel 690	0.05	27-31	7-11	Balance	-	-	0.5	0.015	-	0.5	0.5	-
Inconnel 693	0.15	27-31	2.5-6	Balance	2.5-4	1	0.5	0.01	-	1	0.5	0.5-2.5

1.6. Development of conductive coating

The overlay coatings of $(La,Sr)CrO_3$ was used as protective coating for alloys to prevent Cr volatility. This layer of coating was used on Ducralloy $Cr_5FeY_2O_3$ [36], Ni-Cr alloys (coating method: low pressure plasma spray) [38] and ferritic stainless steels (coating method: spin coated) [40] and improves the electrical performance and surface stability. The $(La,Sr)CoO_3$ coatings were used by E. Batawi, K. Honegger, D. Diethelm and M. Wettstein (coating method: layers thermally sprayed) [41] on Ducralloy $Cr_5FeY_2O_3$ and Ni-Cr alloy. However, this coating increased the oxidation rate of the based units due to the rapid diffusion of chromium though the coating and formation of thick interfacial reaction layers [42]. When compared the $(La,Sr)CrO_3$ and $(La,Sr)CoO_3$ ceramic coating, the Co-containing perovskites provides higher electrical conductivity and oxygen ion conductivity. However, the high oxygen ion conductivity caused high growth rate beneath the protective layer and affect the stability of coating and based substrates [42]. In addition, chromium is transfer easily though the coating and causes fuel cell poisoning.

Spinel type protective coatings including $(Mn,Cr)_3O_4$ and $(Mn,Co)_3O_4$ were also investigated. However, Co-type spinel is more favorable due to volatility of chromium. Different Co-type spinel compositions were investigated. Y. Larring and T. Norby [43] showed the protective layer of $(Mn,Co)_3O_4$ effectively prevent migration and volatility of chromium. Surry coating method was used to formed $Mn_{1.5}Co_{1.5}O_4$ on ferritic stainless steels (i.e. AISI 430 and Crofer 22 APU) and these coated interconnects were used for intermediate temperature SOFCs. X.

Chen, P. Y. Hou, C. P. Jacobson, S. J. Visco and L. C. De Jonghe [44] used slurry coating followed by mechanical compaction and air heating formed $MnCo_2O_4$ on ferritic stainless steel (AISI 430). This coating reduces significantly Cr2O3 sub-scale formation, lower the thermal expansion mismatch, and increase the electronic conductivity of the scale. M. Burriel, G. Garcia, J. Santiso, A. N. Hansson, S. Linderoth and A. Figueras [45] used pulsed injection metal organic chemical vapour deposition formed Co_3O_4 on Fe-22Cr metallic interconnects to be used in intermediate temperature SOFCs. The electrical conductivity of Mn-Co spinel was examined to be 60 Scm^{-1} and is 3-4 and 1-2 orders of magnitude higher than chromia and $MnCr_2O_4$ [41]. This spinel prevent the Cr crossing effectively [46]. The electrochemical performance of SOFCs were test using ferritic stainless steels with $Mn_{1.5}CoO_4$ coating and the results showed long term stability of the $(La,Sr)MnO_3$ cathode.

1.7. New materials for use as interconnects with impure anode feeds

In general, the published research largely describes short term tests and simple fuel chemistry concerning conversion of fuels including a hydrocarbon such as methane or carbon monoxide. However, the mechanism of hydrogen sulfide-induced degradation of many materials used as interconnects/current collectors at the anode sides during SOFCs operation is still not clear.

Most of interconnect/current collector materials discussed above operate in purified hydrogen. These materials can withstand the oxidation at the anode/cathode side but not metal dusting or sulfur corrosion. Some of these alloys (e.g.Inconel 625) form oxide layer (low conductivity) which is not suitable for

their use as current collectors. Thus new approaches are required for use of contaminated fuels, including fabrication of current collectors that can operate in H_2S-containing syngas.

1.8. References

1. S. Ghosh and S. De, *Energy*, **31**, 345 (2006).

2. P. Kuchonthara, S. Bhattacharya and A. Tsutsumi, *Fuel*, **84**, 1019 (2005).

3. R. P. O'Hayre, S.-W. Cha, F. B. Prinz and W. Colella, *Fuel cell fundamentals*, John Wiley & Sons, New Jersey (2006).

4. G. Hoogers, in *Fuel Cell Technology Handbook*, CRC Press (2002).

5. A. B. Stambouli and E. Traversa, *Renewable and Sustainable Energy Reviews*, **6**, 433 (2002).

6. M. Liu, H2S-Powered Solid oxide fuel cells, in *Department of Chemical and Materials Engineering*, University of Alberta, Edmonton (2004).

7. W. Z. Zhu and S. C. Deevi, *Materials Science and Engineering A*, **348**, 227 (2003).

8. Z. G. Yang and J. W. Stevenson, *Advanced Materials & Processes*, **161**, 34 (2003).

9. R. H. Jeffrey Wayne Fergus, Xianguo Li, Jiujun Zhang, *Solid oxide fuel cells -- Materials Properties and Performance*, CRC Press, New York (2009).

10. D. H. Peck, M. Miller and K. Hilpert, *Solid State Ionics*, **123**, 47 (1999).

11. D. H. Peck, M. Miller and K. Hilpert, *Solid State Ionics*, **123**, 59 (1999).

12. S. Onuma, S. Miyoshi, K. Yashiro, A. Kaimai, K. Kawamura, Y. Nigara, T. Kawada, J. Mizusaki, N. Sakai and H. Yokokawa, *Journal of Solid State*

Chemistry, **170**, 68 (2003).

13. S. Miyoshi, S. Onuma, A. Kaimai, H. Matsumoto, K. Yashiro, T. Kawada, J. Mizusaki and H. Yokokawa, *Journal of Solid State Chemistry*, **177**, 4112 (2004).

14. Y. Zhenguo, *International Materials Reviews*, **53**, 39 (2008).

15. Z. Yang, M. S. Walker, P. Singh and J. W. Stevenson, *Electrochemical and Solid-State Letters*, **6**, B35 (2003).

16. S. P. S. Badwal, *Solid State Ionics*, **143**, 39 (2001).

17. D. JR, *ASM Specialty Handbook: Stainless Steels*, ASM International, Materials Park (1994).

18. S. CT, S. NS and H. WC, *Superalloys II*, John Wiley and Sons, New York (1987).

19. P. Kofstad, *Nonstoichiometry, Diffusion, and Electrical conductivity in Binary Metal Oxides*, Robert E.Krieger Publishing Company, Florida (1983).

20. A. Holt and P. Kofstad, *Solid State Ionics*, **69**, 137 (1994).

21. A. Holt and P. Kofstad, *Solid State Ionics*, **69**, 127 (1994).

22. K. Hilpert, D. Das, M. Miller, D. H. Peck and R. Weiss, *Journal of The Electrochemical Society*, **143**, 3642 (1996).

23. N. Q. Minh and T. Takahashi, in *Science and Technology of Ceramic Fuel Cells*, p. 165, Elsevier Science Ltd, Oxford (1995).

24. Q. WJ, S. V and S. L., Materials Used at High Temperatures for a Bipolar Plate of a Fuel Cell, in *U.S. Patent* (2003).

25. J. W. Fergus, *Materials Science and Engineering A*, **397**, 271 (2005).

26. Z. Yang, J. S. Hardy, M. S. Walker, G. Xia, S. P. Simner and J. W. Stevenson,

Journal of The Electrochemical Society, **151**, A1825 (2004).

27. J. Y. Kim, V. L. Sprenkle, N. L. Canfield, K. D. Meinhardt and L. A. Chick, *Journal of The Electrochemical Society*, **153**, A880 (2006).

28. S. P. Simner, M. D. Anderson, G.-G. Xia, Z. Yang, L. R. Pederson and J. W. Stevenson, *Journal of The Electrochemical Society*, **152**, A740 (2005).

29. N. Q. Minh, *Solid State Ionics*, **174**, 271 (2004).

30. Z. Yang, G.-G. Xia and J. W. Stevenson, *Journal of Power Sources*, **160**, 1104 (2006).

31. S. J. Geng, J. H. Zhu and Z. G. Lu, *Electrochemical and Solid-State Letters*, **9**, A211 (2006).

32. S. Jianian, Z. Longjiang and L. Tiefan, *Oxidation of Metals*, **48**, 347 (1997).

33. P. Kofstad, *Oxidation of Metals*, **44**, 3 (1995).

34. D. L. Douglass, P. Kofstad, P. Rahmel and G. C. Wood, *Oxidation of Metals*, **45**, 529 (1996).

35. C. H. Toh, P. R. Munroe and D. J. Young, *Materials at High Temperatures*, **20**, 527 (2003).

36. Z. Zeng and K. Natesan, *Solid State Ionics*, **167**, 9 (2004).

37. N. Jacobson, D. Myers, E. Opila and E. Copland, *Journal of Physics and Chemistry of Solids*, **66**, 471.

38. T. Kadowaki, T. Shiomitsu, E. Matsuda, H. Nakagawa, H. Tsuneizumi and T. Maruyama, *Solid State Ionics*, **67**, 65 (1993).

39. K. Fujita, K. Ogasawara, Y. Matsuzaki and T. Sakurai, *Journal of Power Sources*, **131**, 261 (2004).

40. Y. Zhenguo, *International Materials Reviews*, **53**, 39 (2008).

41. W. J. Quadakkers, H. Greiner, M. Hänsel, A. Pattanaik, A. S. Khanna and W. Malléner, *Solid State Ionics*, **91**, 55 (1996).

42. Y. Larring and T. Norby, *Journal of The Electrochemical Society*, **147**, 3251 (2000).

43. X. Chen, P. Y. Hou, C. P. Jacobson, S. J. Visco and L. C. De Jonghe, *Solid State Ionics*, **176**, 425 (2005).

44. M. Burriel, G. Garcia, J. Santiso, A. N. Hansson, S. Linderoth and A. Figueras, *Thin Solid Films*, **473**, 98 (2005).

45. Z. Yang, G. Xia and J. W. Stevenson, *Electrochemical and Solid-State Letters*, **8**, A168 (2005).

46. S. P. Simner, M. D. Anderson, G.-G. Xia, Z. Yang, L. R. Pederson and J. W. Stevenson, *Journal of The Electrochemical Society*, **152**, A740 (2005).

2.0 The effect of metal dusting/carbon deposition on metals

2.1. Introduction

Metal dusting poses a serious corrosion problem in petro-chemical, energy and in certain chemical industries. For examples, the carbon deposited on the active surface of metal catalyst and caused loss of catalytic activity; the meal dusting and deposited carbon caused plugging in a reactor and decreased the heat transfer properties. Since the 1950's, extensive studies have been made into understanding the phenomenon and development of preventive methods to address the metal dusting/carbon deposition process. The following sections will introduce this subject and review related work by other researchers which is relevant to the present research.

The transition metals such as iron, nickel and cobalt are particularly susceptible to metal dusting. This process occurs at temperatures ranging from 400^{o}C to 800^{o}C in atmospheres containing carbon monoxide or hydrocarbons when their carbon activities are greater than unity, $a_c > 1$ (when hydrocarbon or carbon monoxide is in the gases phase) [1-3]. Under such conditions carbon will form, then transfer into the metal phase which becomes oversaturated. Subsequent growth of graphite will destroy the metal structure [1]. The occurrence of metal dusting depends greatly on the composition of the surrounding atmosphere. In petrochemical industries, a mixture of synthetic gases (i.e. syngas) is often created by reaction of methane, natural gas or coal with steam. Syngas is comprised mostly of H_2, CO, with lesser amounts of CO_2 and H_2O [4] . Coal syngas and biogas, derived from bio-matter, also contains small amounts of H_2S and other

contaminants, in amounts varying from 5 to 300 ppm (Table 2.1). The effect of gas composition (i.e. relative amounts of H_2, H_2S and H_2O) on metal dusting will be discussed in a later section.

Table 2.1. The composition and H_2S concentration for some fuel sources [5].

Fuel type	Typical composition	H_2S concentration
Coal syngas	H_2, CO, CO_2, H_2O, N_2	100-300 ppm
Biogas	H_2, CO, CO_2, H_2O, N_2, CH_4	50-200 ppm
Sour natural gas	CH_4, C_2H_6, CO_2, N_2	>1%

2.2. Mechanism of metal dusting

Many high temperature alloys such as nickel, iron and cobalt are susceptible to carbon deposition but there are some exceptions. Intensive efforts have been made to investigate the process, and these have shown that carbon deposition on metals is primarily a kinetically controlled phenomenon, not thermodynamically controlled [1, 6]. The kinetics of carbon deposition depends on many factors such as mechanism, catalysts for formation of carbon from the source gases, size of reactors, gas flow rates, etc. Therefore the occurrence and formation of carbon are difficult to predict. Two general mechanisms were proposed [6] :

1. The formation of filamentous carbon caused by solid catalyzed reaction.
2. Gas phase pyrolysis caused by formation of graphitic carbon.

The difference between mechanisms (1) and (2) is that in the former carbon is formed inside the metal structure, causing internal stress leading to the disintegration of metal. In the latter, graphitic carbon is formed on the surface of metal without destroying the metal's structure [6].

The mechanisms of carbon deposition on metals are complex and still not well understood [7-9]. Several models have been proposed. One of the most widely accepted theories for carbon deposition in iron based alloys is shown in Fig. 2.1. Initially, the carbon bearing gases are adsorbed (Step 1) on the metal surface, followed by the formation of carbon (Step 2) through the following reactions:

$$2CO_{(g)} \rightarrow CO_{2(g)} + C_{(s)} \quad (2.1)$$

$$CO_{(g)} + H_2 \rightarrow H_2O_{(g)} + C_{(s)} \quad (2.2)$$

$$C_xH_{y(g)} \rightarrow y/2H_{2(g)} + xC_{(s)} \quad (2.3)$$

The carbon activities for Equation (2.1), (2.2) and (2.3) can be calculated from:

$$a_c = K_p \frac{(P_{co})^2}{P_{CO_2}} \quad (2.1a)$$

$$a_c = K_p \frac{P_{co} \cdot P_{H_2}}{P_{H_2O}} \quad (2.2a)$$

$$a_c = \left(K_p \frac{P_{c_xH_y} \cdot}{P_{H_2^{y/2}}} \right)^{1/x} \quad (2.3a)$$

Where K_p is the equilibrium constant showed in Fig. 2.2 [4]. When $a_c>1$, the carbon is transferred into the metal bulk and there is oversaturation of the metal phase. When $a_c=1$ the cementite (M_3C, M=Fe or Ni) formed between the metal and graphite becomes unstable and decomposes to metal and carbon; When $a_c<1$ no metal dusting occurs. For syngas, the carbon is deposited by the Boudouard reaction (Eqn. 2.1) and reduction of CO by H_2 (Eqn. 2.2). Natural gas and higher

carbon bearing gases decompose at high temperature by forming hydrogen and carbon through a sequence of bond-breaking reactions (Eqn. 2.3).

Carbon deposits on the metal (M = iron and nickel) surface, diffuses and reacts with it to form metal carbides:

$$3M_{(s)} + C \rightarrow M_3C \qquad (2.4)$$

In the presence of H_2 and CO:

$$3M_{(s)} + H_2 + CO \leftrightarrow M_3C + H_2O \qquad (2.5)$$

For Fe alloys, surface cementite is formed and acts as a barrier for further transfer of carbon [10]. The carbon activity (a_c) is lower than unity at the Fe_3C/graphite interface and the cementite decomposes into graphite and iron. The cementite acts in three ways [10]: (1) provides a template for graphite nucleation and growth; (2) catalyzes the surface reaction; (3) dissolves and transports carbon. For nickel alloys, metastable Ni_3C is not formed. Since the solubility of carbon in nickel is low, nickel easily becomes supersaturated with carbon followed by profuse graphitization which causes total disintegration of metal [11, 12].

It should be noted that the extent of the coking process can be reduced if the inlet gases contain water [14]:

$$C + H_2O \leftrightarrow H_2 + CO \qquad (2.6)$$

However, excess steam with a ratio of steam to carbon up to 3 is needed to completely prevent coking. In actual practice, it is not practical to use large amounts of stream as this may cause oxidation of metals [14]. The growth of carbon and metal carbide will push the metal particles out from the metal surface. Excess hydrogen content in syngas weakens the grain boundaries of metal by

diffusing into them, causing metal detachment from the surface and thus destruction of its structure [3]. The gases continue to absorb and form metal carbides on the surface of metals until its break-up (Step 5 to Step 7 in Fig. 2.1). The metal carbides act as reaction sites for the growth of carbon filaments (Step 8) [9] .

Step 1: Gas adsorption on the metal surface.

Step 2: Separation of carbon.

Step 3: Carbon diffuses into metal.

Step 4: Metal carbides are created.

Step 5: Gases continue to adsorb on the surface of metal carbides.

Step 6: Repeat of Step 1 to Step 5.

Step 7: Surface break-up.

Step 8: Carbon filaments grow.

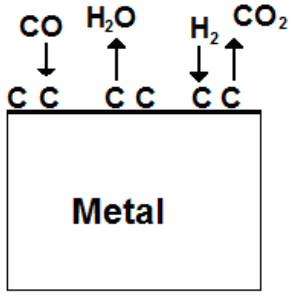

Step 1 to step 2

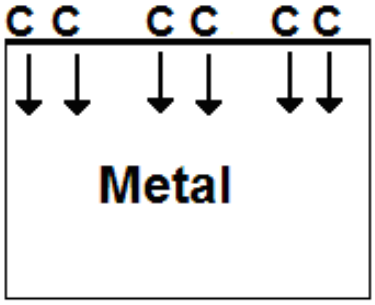

Step 3

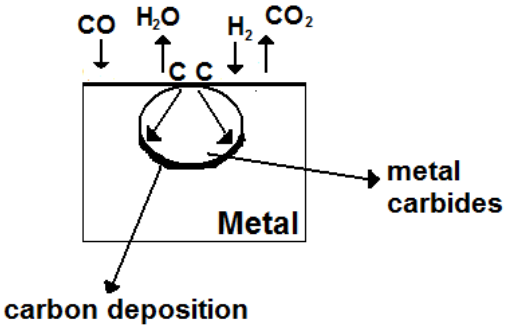

Step 4, Step 5 and Step 6

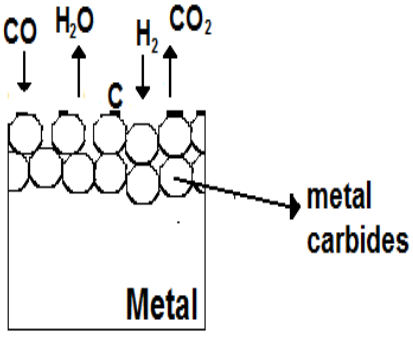

Step 7

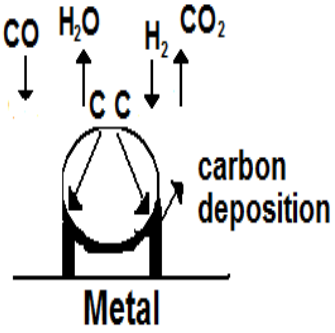

Step 8

Figure 2.1. The mechanism of carbon deposition on metal [1-3, 11, 13].

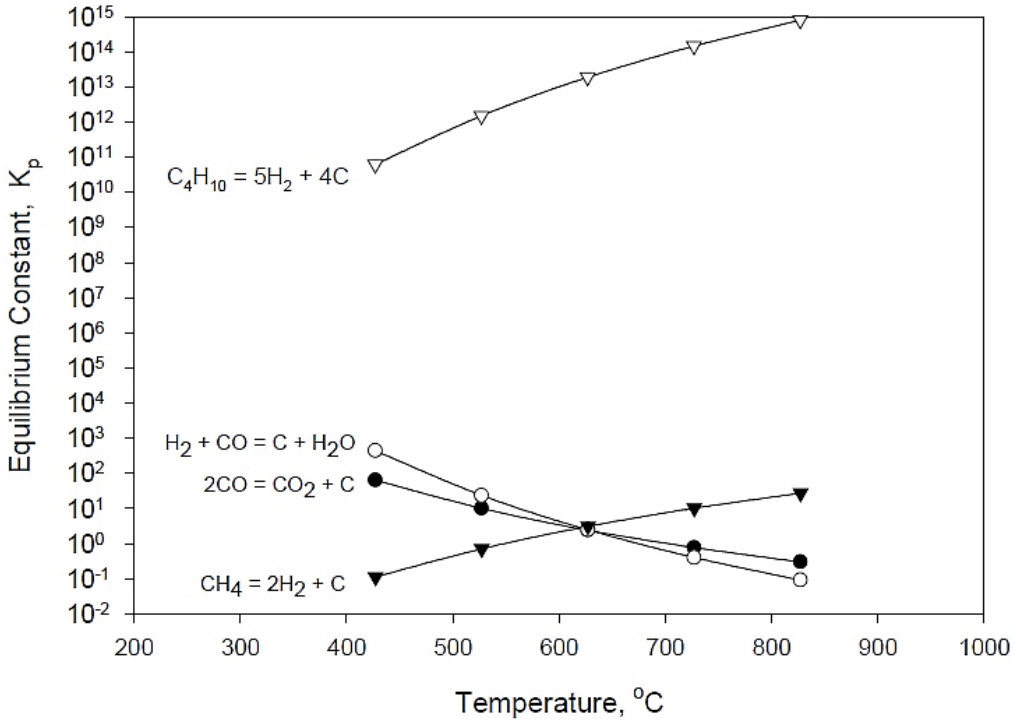

Figure 2.2. The equilibrium constant as a function of temperature for carbon formation from various carbon bearing gases [4].

Nickel-based alloys show slower metal dusting process when compared to Fe-based alloys (Fig. 2.3). The metal dusting and growth of graphite on Ni and Ni-based alloys occurred internally and caused extrusion and ejection of metal particles [15]. The metal dusting of iron/steel forms smaller particles (~ 20 nm) as a consequence of formation of intermediate carbide [1, 15]. The relatively larger nickel particles are less reactive than Fe particles which lead to slower carbon deposition on nickel and its alloys. The resistance against metal dusting for Ni-based alloys is better than for Fe-based alloys (steels) due to [1, 16]: 1. slower carbon formation; 2.fewer carbon filaments formed; 3.carbon solubility and carbon diffusion are lower. Many studies showed that no nickel carbides (i.e.Ni_3C) were detectable in a highly carburizing gas atmosphere [17]. The metastable Ni_3C

decomposed into Ni and C at high temperature (> 650 ^{o}C) [18, 19].

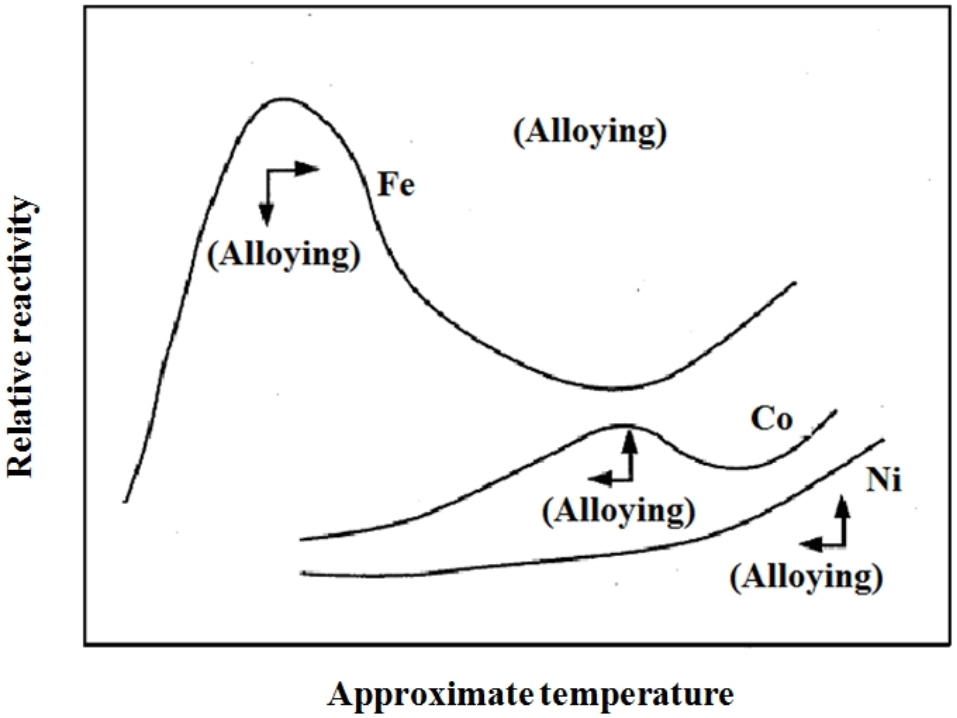

Figure 2.3. Schematic representation of reactivity vs increasing temperature for pure iron, nickel and cobalt in 1 atm of pure CO.

Sacco et al. [20] reported that there were a shift in the relative intensity of the diffraction lines of nickel foil after exposure to carbon bearing gases. This showed that there are preferential plane orientations important for carbon deposition on nickel. Some planes are more active and thus are selectively covered by carbon [10, 21, 22]. There is: no carbon coverage on nickel (001); full coverage by carbon on nickel (111) and partial coverage by carbon on (101) and other faces [10, 22]. Although the orientation of nickel crystal planes affects the carbon deposition process, this is not the case for metal dusting [1, 23-25]. On (111) planes of nickel, the graphite layers form parallel to the metal surface and cause no direct metal dusting, whereas on the nickel (100) plane the layers grow into the

metal phase and lead to destruction of nickel structure.

2.3. Metal dusting on copper and copper-nickel alloys

Copper and copper-based alloys resist metal dusting more effectively than nickel and its alloys [10, 26-31]. Copper has no catalytic effect on the decomposition of hydrocarbons [3, 31] due to the extremely low solubility of carbon in copper [32]. The rate of metal dusting found for nickel can be reduced by alloying it with copper. While copper generally is inert as a catalyst for decomposition of hydrocarbons some researchers detected formation of carbon nanotubes on pure copper surfaces [32, 33]. The carbon filaments were extremely small and even after 150 h reaction still could not be detected by XRD.

In general, alloying nickel with copper decreases the rate of carbon deposition. The carbon uptake on the surface of copper-nickel alloy became less with increasing of copper content (Fig 2.4). By alloying nickel with more than 20 wt% of copper, the carbon uptake became negligible [32] .

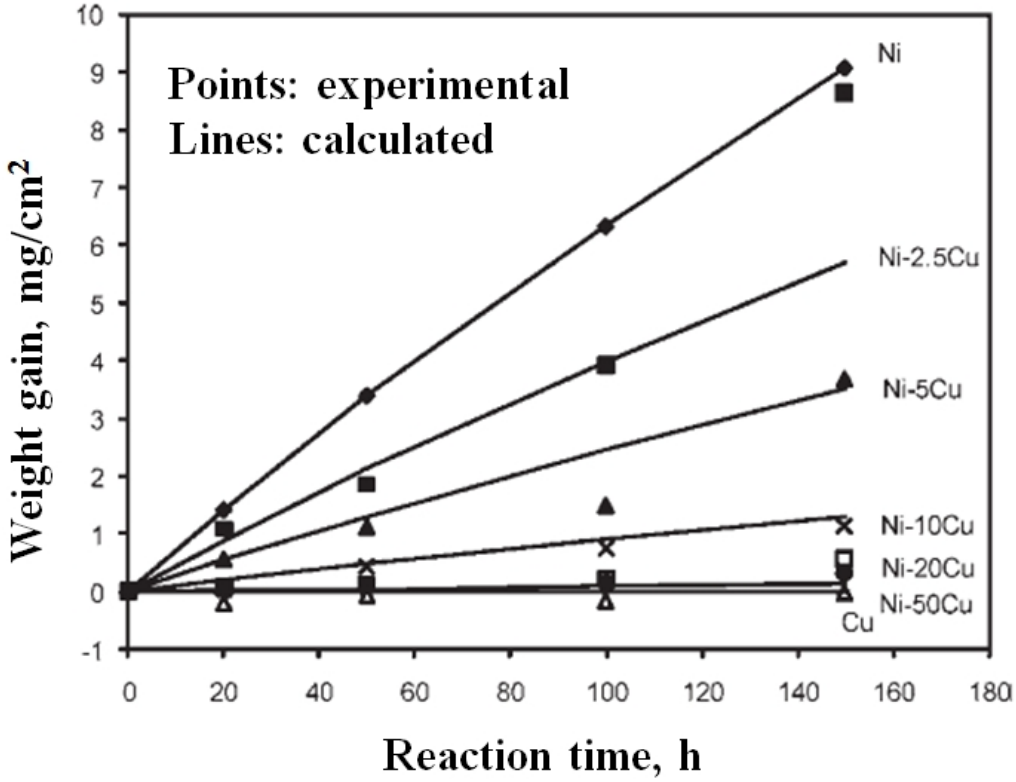

Figure 2.4. The effect of alloying copper with nickel on the carbon uptake in the gas mixture 68%CO–31%H_2–1%H_2O [10]. The value of *X* expresses the percentage of copper in an alloy Ni-*X*Cu.

Nishiyama et al. [29] examined the effects of hydrogen on carbon deposition catalyzed on copper-nickel alloys using benzene-hydrogen-helium gas mixtures at 700^{o}C. For pure nickel, the carbon deposition rate increased with increasing concentration of hydrogen. Hydrogen catalyzed the coking process on the nickel-rich substrate by removing the surface carbon films. Upon removal of the surface carbon film, the active nickel sites become exposed to further hydrocarbon and form new carbon. Hydrogen removed the chemisorbed species which are the precursor of the deposition. Hydrogen dissolves in the nickel but this process does not affect the diffusion of carbon atoms into the metal. However, the dissolved

hydrogen loosens the grain boundaries of the metal and so causes detachment of metal particles. The detachment of metal particles increases the active surface area, which also leads to both metal dusting and increased carbon deposition rate.

The carbon deposition rate on metals is significantly affected by the presence of hydrogen [34-36]. Yoshida et al. [36] pointed out that when $P_{H2}/P_{CO} < 1$ the carbon forming reactions are:

$$CO + H_2 \rightarrow C + H_2O \quad (2.7)$$

$$2CO \rightarrow C + CO_2 \quad (2.8)$$

The rate of reaction (2.7) is proportional to the amount of H_2. Reaction (2.8) occurs in relative low partial pressures of H_2. The findings suggest that hydrogen creates free nickel surface area by reacting with carbon and the formation of volatile products. For example, H_2 reacts with carbon to form CH_4 with consequent increase in the free surface area of nickel [36, 37].

2.4. Protection against metal dusting

A metal and its alloys can be protected against metal dusting on its surface by one or more of the following methods [1, 2, 16, 38-40]:

(1) poisoning the active sites at the metal surface with sulfur;

(2) sealing the surface of the metal by formation of a layer of metal oxide such as Cr_2O_3 and Al_2O_3;

(3) coating the metal with a layer of a different metal which is inactive for catalytic decomposition of hydrocarbons.

Sulfur is adsorbed strongly on several different metal surfaces and interrupts the mechanism of carbon deposition through blocking of one or more steps. As

discussed above, the diffusion of carbon into the metal is an important step in the metal dusting process; a layer of oxide or inactive metal coating can prevent the carbon diffusion when there are no pores or cracks. Thus there are three ways to protect nickel foam from carbon deposition. Each of the above methods has its advantages and disadvantages, which will be discussed in detail in the following section.

2.4.1. Preventing metal dusting by oxide films

The oxygen partial pressure in the CO-H_2-H_2O mixture is not sufficient to oxidize Fe and Ni [4, 16, 41, 42]. However, elements such as Cr, Mn, Al, etc. can be oxidized and form protective oxide layers against metal dusting. Low alloy steels, which are heat and oxidation resistant, have resistance to metal dusting up to 600^{o}C if the partial pressure of oxygen is high enough to form magnetite [39]. High alloy steels with Cr content greater than 11% are more resistant to metal dusting. The high Cr content causes high Cr diffusivity in the ferritic lattice and forms outer (spinel, $MnCr_2O_4$ and $FeCr_2O_4$) and inner (chromia, Cr_2O_3) oxide protective layers [39].

However, the protective oxide layer formed in high alloy steels still is subject to metal dusting after long exposure to metal dusting conditions due to localized attacks at weak points (Fig. 2.5):

1. A protective oxide layer is formed.
2. Weak points or cracks are formed in the oxide layer. These cracks are formed by intrinsic oxide growth stresses [10].
3. The carbon accesses bare metal surface by diffusion through the cracks.

4. The carbon reacts with the alloying elements to form stable carbides: for elemental Cr, $M_{23}C_6$ and M_7C_3; MC when M= Ti, Zr, V, Nb, W; and Mo_2C.
5. Very fine domains of internal carbide are formed and the zone becomes oversaturated with dissolved carbon. The metal matrix then disintegrates and forms fine metal particles.
6. The ejected metal particles act as catalyst for carbon deposition.

Both low and high alloy steels are susceptible to metal dusting. The low alloy steels follow the mechanism of Fe-alloy. For high alloy steels, a protective oxide (Cr_2O_3) can retard metal dusting, but this depends on their ability to form and heal the chromia layer. The protective oxide layer is difficult to form due to the low diffusivity of Cr [15, 16, 35, 41, 43-48]. The effect of the metal dusting in high alloy steels appears mainly as pitting. Stable carbides (e.g.M_7C_3 and $M_{23}C_6$) can be formed within the high alloy steel, which causes destruction of the metal [38, 41, 42]. The rates of carbon forming reactions on both low and high alloy steels depend on the catalytic activity of the metal particles.

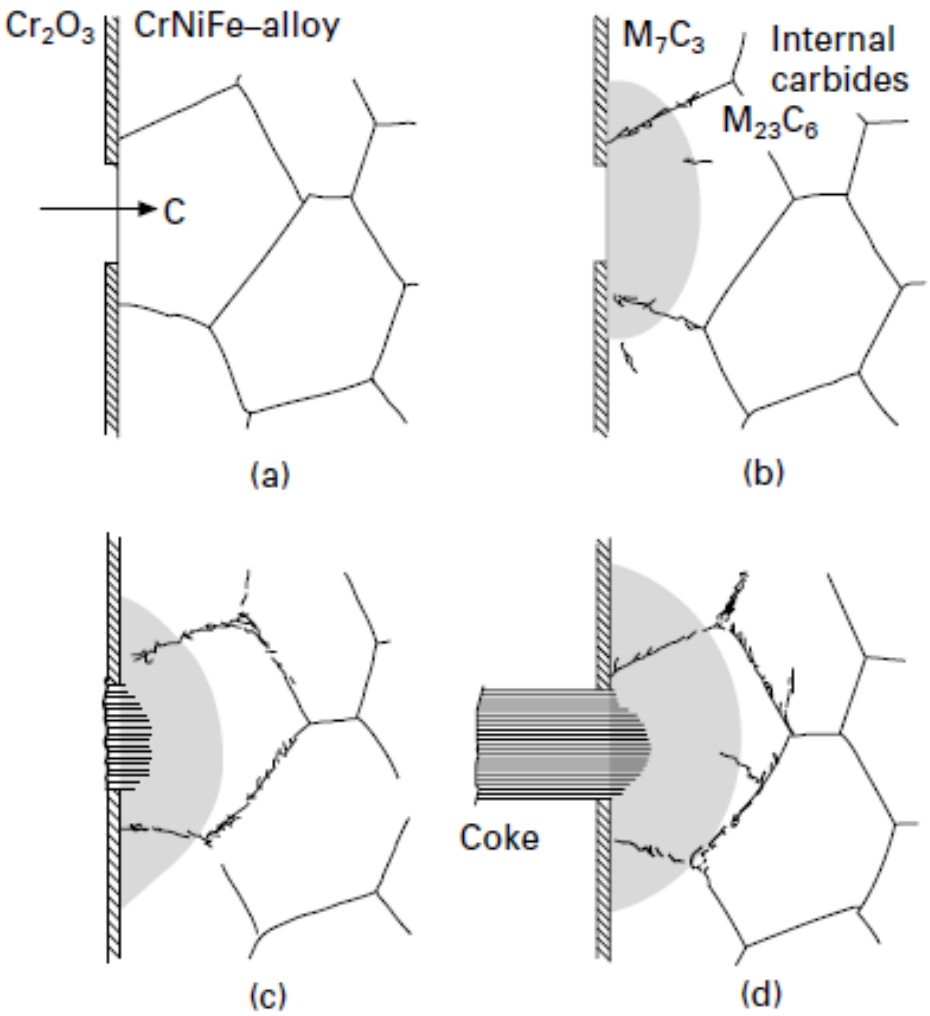

Figure 2.5. Metal dusting on chromia forming high-alloy steels [1].

2.4.2. Influence of H_2S on metal dusting

Metal dusting can be prevented in the presence of H_2S [1, 2, 39-41, 45, 49]. The effect of H_2S on metal dusting of iron is a function of temperature and the ratio of P_{H2S}/P_{H2} (Fig. 2.6) [1] :

$$H_2S = H_2 + S \text{ (adsorbed)} \qquad (2.9)$$

In the presence of H_2S, the sulfur is adsorbed on the metal surface and hinders the transfer of carbon into metal solid solution. The adsorbed sulfur protects the active surfaces against reactions which can catalytically decompose CO or

hydrocarbons. The C containing molecules cannot be adsorbed onto the sulfided surface, and so are not dissociated, since the adsorption sites are occupied by sulfur. However, even with a high partial pressure of H_2S, P_{H2S}, a portion of the active sites of metal are not completely covered by sulfur and metal dusting occurs after long exposure to H_2S-containing carburizing atmospheres. Fig. 2.7 compares metal dusting on iron in atmospheres with and without H_2S: (1) The iron surface first is poisoned by sulfur; (2) after a long period, metal dusting starts; then (3) when the surface is blocked by sulfur, metal dusting (e.g.cementite for iron alloys) starts below the sulfur layer. For nickel, the catalytic decomposition of CO or a hydrocarbon is not possible when the fractional coverage (θs) is at least 0.7-0.8 [50]. However, in this case the nickel loses its catalytic activity.

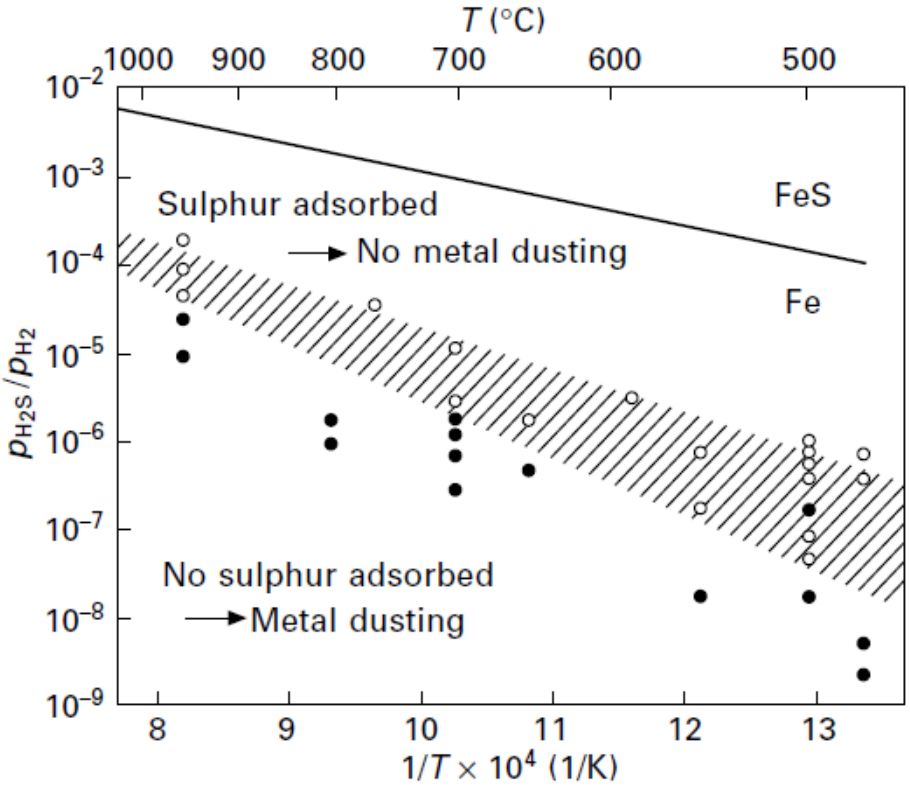

Figure 2.6. Influence of H_2S on metal dusting [40].

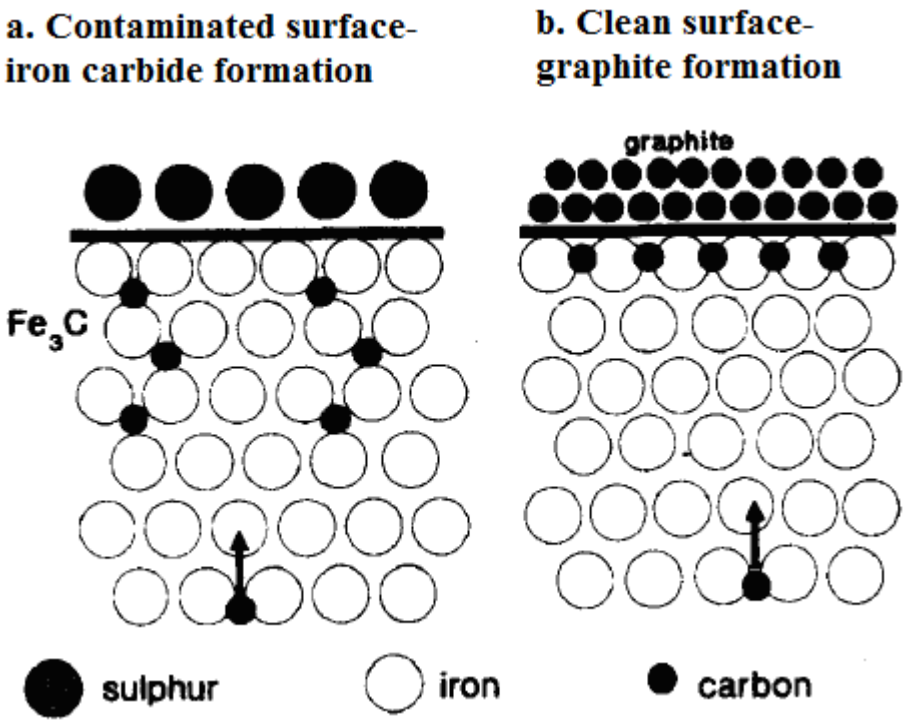

Figure 2.7. The influence of H_2S on metal dusting of iron [1].

2.4.3. Material choice selection for current collectors in SOFCs

The crucial roles of the current collector in SOFCs fuel cell are to collect and distribute the electrons so as to generate electrical current. Thus it must be able to conduct electrons. Therefore neither a non-conductive oxide layer nor a protective layer of sulfur can serve as the protective layer for nickel foam, since the oxide layer formed on nickel has low electronic conductivity. The conductivity of nickel foam is decreased when the metal surface is covered with a monolayer of adsorbed sulfur. Consequently it is necessary to protect the surface of nickel foam using a material which is both conductive and resistant to coking.

2.5. References

1. H. J. Grabke and M.Tze, Corrosion by Carbon and Nitrogen - Metal Dusting, Carburisation and Nitridation (EFC 41), in, Woodhead Publishing.

2. R. F. Hochman and J.H.Burson, in *API Division of Refining Proceeding*, p. 331 (1966).

3. A. I. La Cava, C. A. Bernardo and D. L. Trimm, *Carbon*, **20**, 219 (1982).

4. B.A. Baker and G. D. Smith, Metal dusting in a laboratory environment-alloying addition effects, in *International Workshop on Metal Dusting*, p. 26, Argonne (2001).

5. M. Gong, X. Liu, J. Trembly and C. Johnson, *Journal of Power Sources*, **168**, 289 (2007).

6. K. Huang and J. B. Goodenough, *Solid oxide fuel cell technology : principles, performance and operations* CRC Press, NW (July 2009).

7. R. T. K. Baker, M. A. Barber, P. S. Harris, F. S. Feates and R. J. Waite, *Journal of Catalysis*, **26**, 51 (1972).

8. A. Sacco, P. Thacker, T. N. Chang and A. T. S. Chiang, *Journal of Catalysis*, **85**, 224 (1984).

9. Y. Sone, H. Kishida, M. Kobayashi and T. Watanabe, *Journal of Power Sources*, **86**, 334 (2000).

10. D. J. Young, J. Zhang, C. Geers and M. Schütze, *Materials and Corrosion*, n/a (2010).

11. Z. Zeng, K. Natesan and V. A. Maroni, *Oxidation of Metals*, **58**, 147 (2002).

12. C. M. Chun, T. A. Ramanarayanan and J. D. Mumford, *Materials and Corrosion*, **50**, 634 (1999).

13. J. Rostrup-Nielsen and D. L. Trimm, *Journal of Catalysis*, **48**, 155 (1977).

14. E. R. Riegel, *Kent and Riegel's handbook of industrial chemistry and*

biotechnology, Springer, New York (2007).

15. S. Strauß, R. Krajak and H. J. Grabke, *Materials and Corrosion*, **50**, 622 (1999).

16. J. Klöwer, H. J. Grabke and E. M. Müller-Lorenz, *Materials and Corrosion*, **49**, 328 (1998).

17. R. T. K. Baker, P. S. Harris, R. B. Thomas and R. J. Waite, *Journal of Catalysis*, **30**, 86 (1973).

18. N. A. Jarrah, F. Li, J. G. Van Ommen and L. Lefferts, *Journal of Materials Chemistry*, **15**, 1946 (2005).

19. N. A. Jarrah, J. G. van Ommen and L. Lefferts, *Journal of Catalysis*, **239**, 460 (2006).

20. A. Sacco, F. W. A. H. Geurts, G. A. Jablonski, S. Lee and R. A. Gately, *Journal of Catalysis*, **119**, 322 (1989).

21. P. E. Nolan, D. C. Lynch and A. H. Cutler, *The Journal of Physical Chemistry B*, **102**, 4165 (1998).

22. J. Zhang, C. Kong and D. J. Young, *Materials at High Temperatures*, **26**, 45 (2009).

23. J. M. Blakely, *Critical Reviews in Solid State and Materials Sciences*, **7**, 333 (1978).

24. Q. Wei, E. Pippel, J. Woltersdorf, S. Strauß and H. J. Grabke, *Materials and Corrosion*, **51**, 652 (2000).

25. C. M. Chun, J. D. Mumford and T. A. Ramanarayanan, *Journal of The Electrochemical Society*, **147**, 3680 (2000).

26. I. Alstrup, *Journal of Catalysis*, **109**, 241 (1988).

27. Y. Nishiyama, K. Moriguchi, N. Otsuka and T. Kudo, *Materials and Corrosion*, **56**, 806 (2005).

28. Y. Nishiyama and Y. Tamai, *Journal of Catalysis*, **33**, 98 (1974).

29. Y. Nishiyama and Y. Tamai, *Journal of Catalysis*, **45**, 1 (1976).

30. E. W. Park, H. Moon, M.-s. Park and S. H. Hyun, *International Journal of Hydrogen Energy*, **34**, 5537 (2009).

31. V. J. Kehrer and H. Leidheiser, *The Journal of Physical Chemistry*, **58**, 550 (1954).

32. J. Zhang, D. M. I. Cole and D. J. Young, *Materials and Corrosion*, **56**, 756 (2005).

33. C. A. Bernardo, I. Alstrup and J. R. Rostrup-Nielsen, *Journal of Catalysis*, **96**, 517 (1985).

34. D. Bianchi and C. O. Bennett, *Journal of Catalysis*, **86**, 433 (1984).

35. P. L. Walker, J. F. Rakszawski and G. R. Imperial, *The Journal of Physical Chemistry*, **63**, 133 (1959).

36. N. Yoshida, T. Yamamoto, F. Minoguchi and S. Kishimoto, *Catalysis Letters*, **23**, 237 (1994).

37. D. L. Trimm, *Catalysis Reviews: Science and Engineering*, **16**, 155 (1977).

38. H. J. Grabke, *Materials and Corrosion*, **49**, 303 (1998).

39. H. J. Grabke, *Materials and Corrosion*, **54**, 736 (2003).

40. A. Schneider, H. Viefhaus, G. Inden, H. J. Grabke and E. M. Müller-Lorenz, *Materials and Corrosion*, **49**, 336 (1998).

41. H. J. Grabke, R. Krajak and E. M. Müller-Lorenz, *Materials and Corrosion*, **44**, 89 (1993).

42. H. J. Grabke, *CORROSION*, **51**, 711 (1995).

43. P. L. Walker, J. F. Rakszawski and G. R. Imperial, *The Journal of Physical Chemistry*, **63**, 140 (1959).

44. G. W. Meetham, *High-Temperature Materials*, Wiley-VCH Verlag GmbH & Co. KGaA (2000).

45. M. Maier, J. F. Norton and P. D. Frampton, *Materials and Corrosion*, **49**, 330 (1998).

46. R. A. Holm and H. E. Evans, *Materials and Corrosion*, **38**, 219 (1987).

47. R. A. Holm and H. E. Evans, *Materials and Corrosion*, **38**, 224 (1987).

48. R. A. Holm and H. E. Evans, *Materials and Corrosion*, **38**, 166 (1987).

49. Hans Jürgen Grabke, E. M. Müller-Lorenz and A. Schneider, *ISIJ International*, **41**, S1 (2001).

50. J. R. Rostrup-Nielsen, *Journal of Catalysis*, **85**, 31 (1984).

3.0 Thesis objectives and motivations

The main objective of this research was to develop conductive/protective coatings for Ni foam to use as current collectors in H_2S-containing syngas at the anode of SOFCs. Such coatings are expected to improve the metal dusting resistance and hydrogen sulfide corrosion resistance as well as the electronic conductivity of the nickel foam substrates.

Three different protective coatings were used: (1)copper coated nickel foam; (2) copper-ceria coated nickel foam; (3) TiO_2 coated nickel foam. Protective coatings (1) and (2) were used to withstand H_2S up to 500 ppm. Protective coating (3) was used to withstand H_2S up to 5000 ppm. Electrodeposition and co-electrodeposition were used for protective coatings (1) and (2). Electrodeposition and co-electrodeposition is technically easy and inexpensive. Dense, adherent, fine-grained and uniform coatings of copper can be achieved. Co-deposition of inert particles (CeO_2) with copper is straightforwardly practical and has been widely studied.

Electrophoretic deposition technique was used for protective coating (3). Although TiO_2 does not show high conductivity, the protective coating (3) is a preliminary method used to understand the electrophoretic deposition process on three-dimensional structure of nickel foam. If this method is successful, other stable and conductive ceramic coating will be used to apply on nickel foam.

4.0 Material stability test methods

4.1. Gravimetric testing method

The gravimetric method is widely used to study high temperature corrosion. This method can continually measure the sample's weight changes as a function of time. Different corrosive gases or mixture of gases can be used for this setup and the mechanism/kinetics of high temperature corrosion can be tested [1]. This is the most widely used method in high temperature corrosion.

The method gives excellent measurement of the sample's weight changes as a function of time. However, this method may not suitable for this research. The corrosive gas mixture of H_2S-syngas was used in this research. Weight gained due to carbon deposition and weight loss due to disengagement of metal particles can occur simultaneously in the process. Therefore, the gravimetric method may not be able to detect these changes. The ability to conduct electricity is the important requirement for the protective coating used in this research. This method is not capable to detect the change. For example, if an alumina forming alloy was tested, the alumina (Al_2O_3) forms a protective layer for alloy but it is not able to conduct electricity and makes it unsuitable to use as current collector.

4.2. Fuel cell testing method

The fuel cell testing method (Fig. 4.1) is suitable for the application. If coated current collectors and gold current collectors have similar power density, the coated current collectors can be consider stable in the corrosive environment. The power density for gold current collectors in SOFC is used as the standard for comparison since gold is stable in a H_2S-syngas atmosphere. The shortcoming of

this setup is that stable anode, cathode and electrolyte are required. This measurement depends on the both ceramic cells and also current collectors. The ceramic cell must be stable in order to confirm the stability of the current collector. For example, if the measured current density is low, this may be due to degradation of the ceramic cells or the degradation of the current collectors.

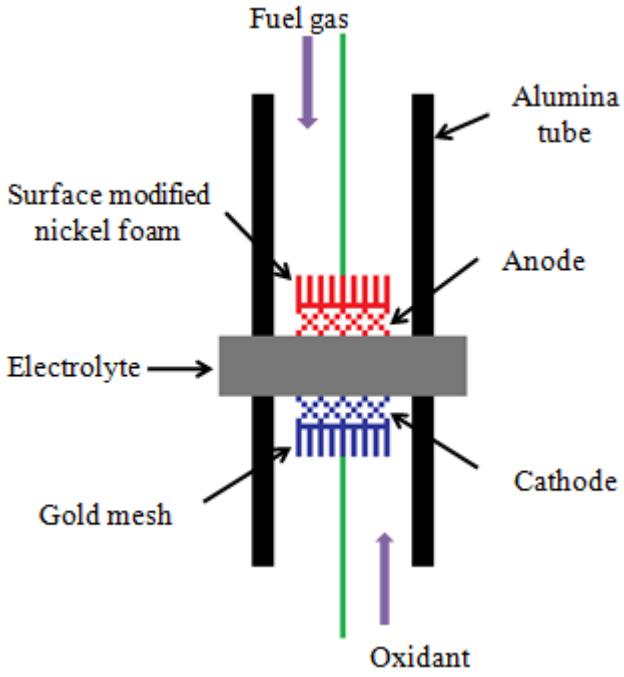

Figure 4.1. Schematic of fuel cell testing method.

4.3. Van der Pauw 4 point conductivity measurement

Van der Pauw 4 point conductivity measurement is commonly used to measure the electronic conductivity of the samples [2, 3]. From Figure 4.2, the sample is located on the Al_2O_3 support and 4 point contacts are placed at the edges of the sample. The 4 point contacts are made from gold (it is inert to H_2S corrosion). The spring connections are used to fix the sample and gold contacts in the right places. The Van der Pauw method provides very accurate conductivity measurement for thin sample. This method is able to measure the conductivity of

the samples as a function of time. This method is able to detect the formation of non-conductive materials formed on the surface of samples. For example, an alumina forming alloy is stable in a H_2S-syngas but the protective layer (Al_2O_3) formed is non-conductive and the Van der Pauw 4 point probe method is able to detect the loss of conductivity. The Van der Pauw method was chosen as the stability testing method in this research because it can monitor both electronic conductivity and stability of the samples is important.

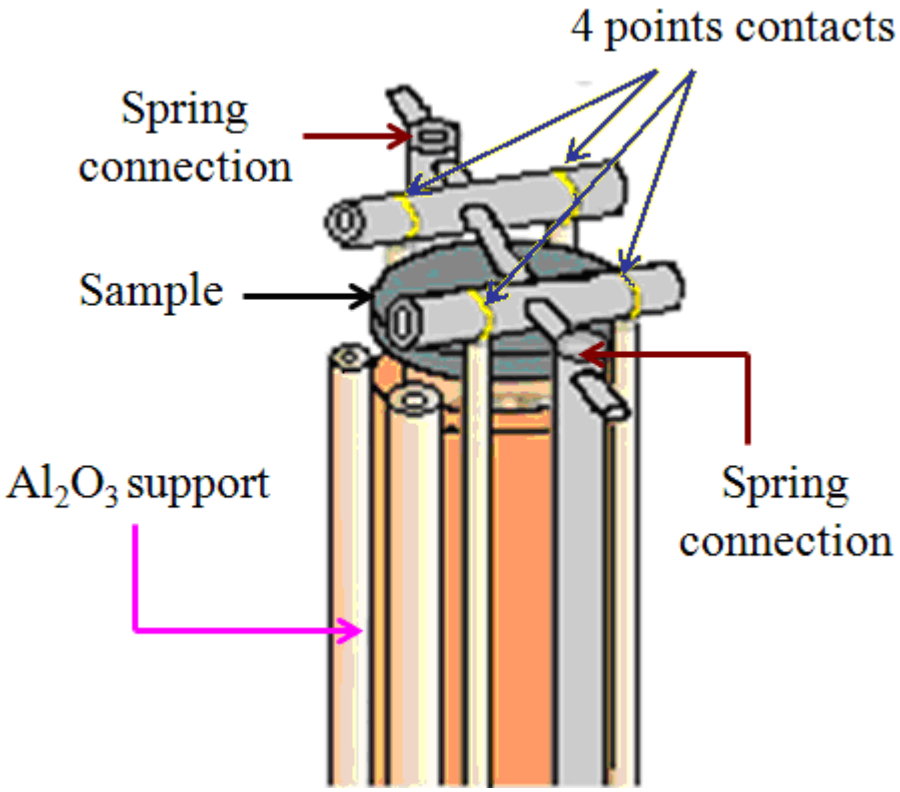

Figure 4.2 The schematic of Van der Pauws 4 points conductivity method.

4.5. References

1. G. Y.Lai, *High-temperature Corrosion of Engineering Alloys*, The Materials Information Society, Ohio (1990).

2. X. C. Tong, *Advanced Materials for Thermal Management of Electronic Packaging*, Springer, New York (2010).

3. L. J. v. d. Pauw, *Philips Research Report*, **13**, 1 (1958).

5.0 Copper coated nickel foam as sulfur and carbon resistant current collector for H_2S-containing syngas solid oxide fuel cells*

5.1. Introduction

In this section, we investigate the properties of copper coated nickel foam as a current collector for practical applications of SOFCs in H_2S-containing syngas at intermediate temperature (750 ^oC). The dependence of carbon deposition and H_2S corrosion on different Cu/Ni ratios was also determined.

5.2. Experimental

5.2.1. Sample preparation and characterization

A traditional electrodeposition technique (Table 5.1) was used to coat both nickel foil and nickel foam with copper. The nickel foam was INCOFOAM®, a commercial product from Vale Canada Ltd. Before electroplating, samples of nickel foil or nickel foam were cleaned with ethanol and acetone, and then rinsed with deionized water. The amount of copper deposited was determined by weighing the nickel foil or nickel foam before and after coating. After completion of the deposition procedure, the copper coated nickel samples were heated at 750 ^oC for 20 h in 5% H_2 (balanced with N_2) and cooled down before either stability testing or electronic conductivity measurement.

The weight of copper coating was calculated using the following equation:

$$\text{Weight of deposited copper (g)} = It \times \frac{1}{\mathrm{F}} \times \frac{1}{2} \times M \qquad (5.1)$$

where I is the deposition current, F is the Faraday constant, 96485 C/mol, t is the deposition time, and M is the atomic weight of copper. The average thickness of

** A version of this chapter has been submitted to Applied Surface Science for publication (under review).*

copper coating was calculated using the following equation:

$$\text{Copper coating thickness} = \frac{\text{deposition weight}}{\rho \times 2 \times \text{A}} \qquad (5.2)$$

where ρ is the density of copper, and A is the surface area of nickel before coating.

The surface and cross section morphologies of the uncoated and copper coated nickel were examined using a Hitachi S-2700 scanning electron microscope (SEM, emission energy =20 kV, working distance = 15-25mm and current = 10-20 mA) equipped with energy dispersive X-ray (EDX). The phase structures of materials were identified using a Rigaku Rotaflex X-ray diffractometer (XRD) with Co Kα radiation.

Table 5.1. The electroplating parameters used for copper deposition.

Parameters	Values
Copper(II) sulfate $CuSO_4 \cdot xH_2O$	180 g/L
Sulfuric acid (H_2SO_4)	60 g/L
Anode	Copper, 30 mm × 60 mm
Cathode	Nickel foil/foam
Temperature	Room temperature
Current density	10 mA/cm^2
Average deposition area	7.14 cm^2
Deposition time	Varied between 30 min and 16 h

5.2.2. Stability of copper coated nickel in carbon or H_2S-containing gas

The stabilities of copper coated nickel samples in syngas or H_2S-containing syngas at high temperature were evaluated by heating them in a quartz tube under flowing gas at a flow rate of 50 cm^3/min at 750 ^{o}C. During sample heating and

cooling at 3^{o}C/min nitrogen gas was used to prevent reactions of the samples at temperatures other than that prescribed. The gases selected for stability tests were introduced into the quartz tube after the measured temperature in the quartz tube was stable at 750 ^{o}C for 30 min.

5.3. Results and Discussion

5.3.1. Characterization of copper coated nickel foils

Copper was deposited successfully on both sides of the nickel foil. Before heat treatment, the actual measured weight and calculated weight based on Equation (5.1) of deposited copper were consistent (Fig. 5.1). The SEM images of the cross sections of the coatings (Fig. 5.2) showed that uniform copper coating layers were obtained on both sides of nickel foil and formed distinct copper layers. The thickness of copper coating was about 118μm (Fig. 5.2b) in good agreement with the calculated coating thickness (Equation 5.2).

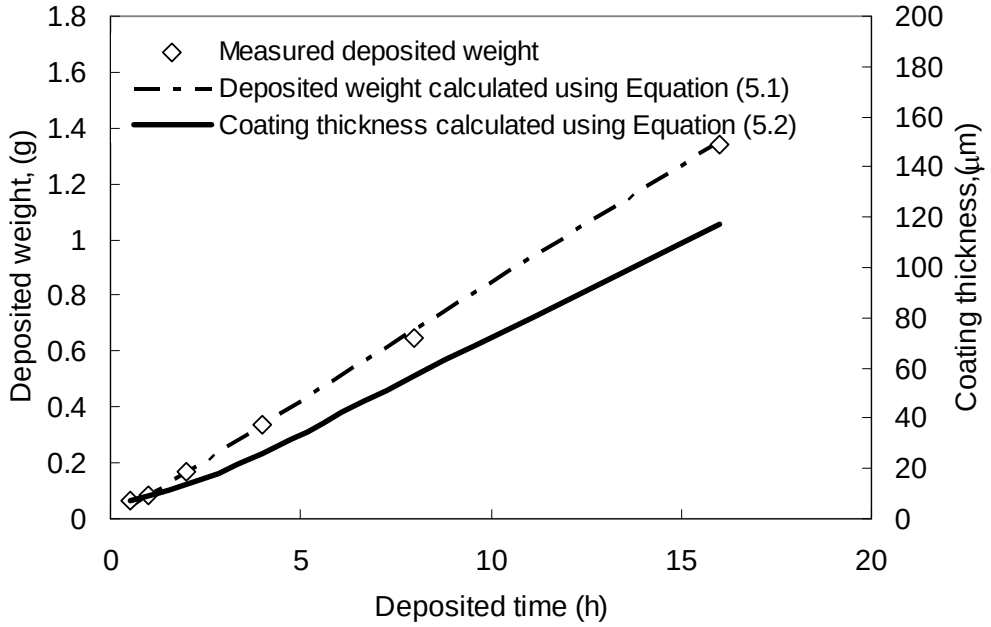

Figure 5.1. Deposited weight and thickness of copper coated nickel as a function of deposition time.

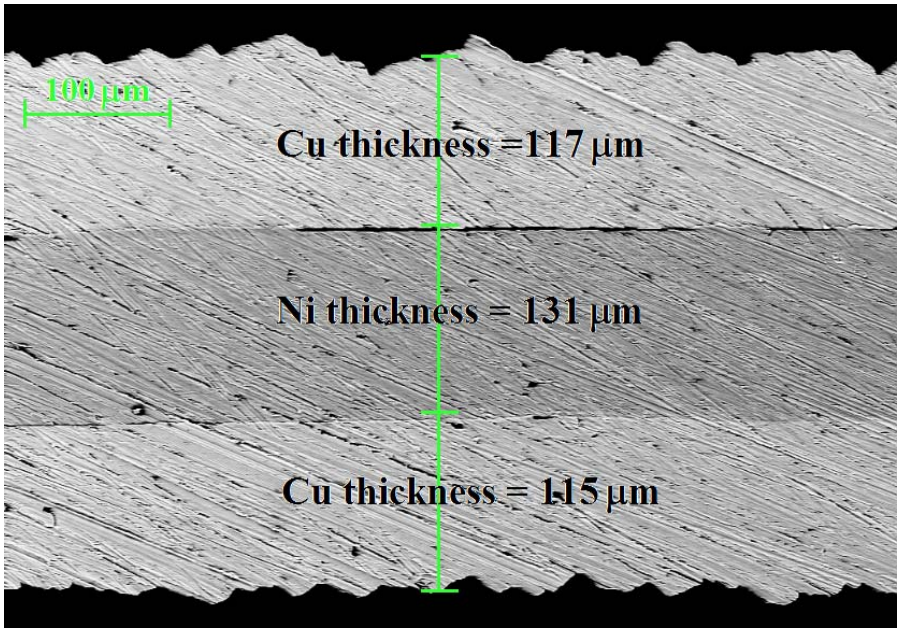

(a) Before heat treatment in 5 % H_2 at 900^{o}C.

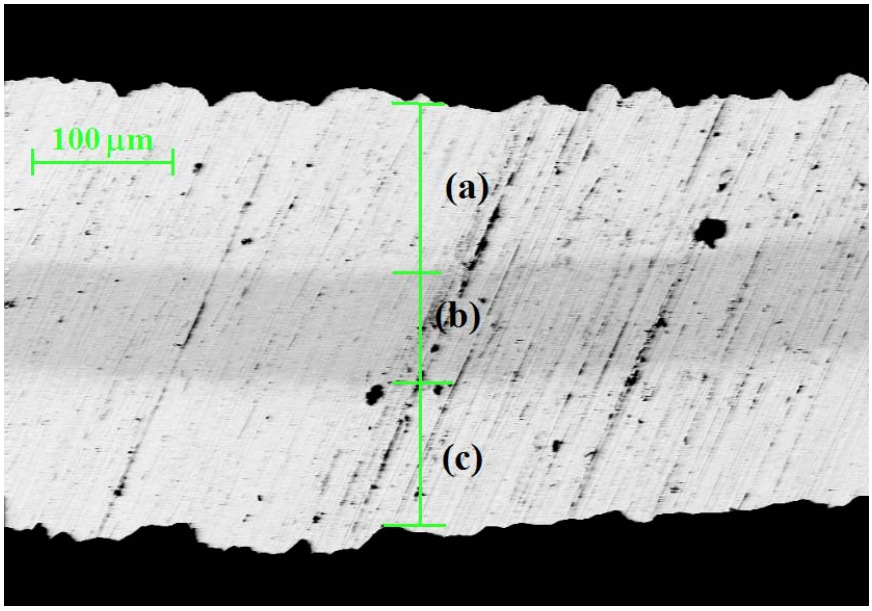

(b) Layers (a), (b) and (c) formed Cu-Ni alloy after heating in 5 % H_2 at 900^{o}C.

Figure 5.2. SEM images (Back-scatter emission, BSE) of the copper coated nickel.

The XRD analysis of copper coated nickel foil (Cu/Ni weight ratio = 0.4) before and after heating at high temperature in reducing atmosphere confirmed copper-nickel alloy formation (Fig. 5.3) as described in earlier report [1]. It should be noted that although the deposited copper layer and nickel substrate have similar thicknesses (Fig. 5.2), the intensities of copper peaks are greater than those for nickel foil due to the "covering effect" of copper outer layer. Diffusion of copper and nickel atoms resulted in the nickel-copper alloying. The high temperature treatment and formation of alloy not only increased the adhesive force of the copper layer onto nickel but also enhanced the homogeneity of the alloy [2]. Although copper-nickel alloy was detected in the XRD pattern (Figure 5.3), the copper coated nickel foam is not completely alloyed. The formation of copper-nickel alloy depends on the heating temperature, the diffusion of the atom and the thickness of the coating. The SEM images of copper coated nickel foil (Cu/Ni weight ratio =1.5) before and after high temperature heating in reducing atmosphere confirmed the diffusion of copper and nickel after high temperature heating (Fig. 5.2(a) and Fig. 5.2(b))

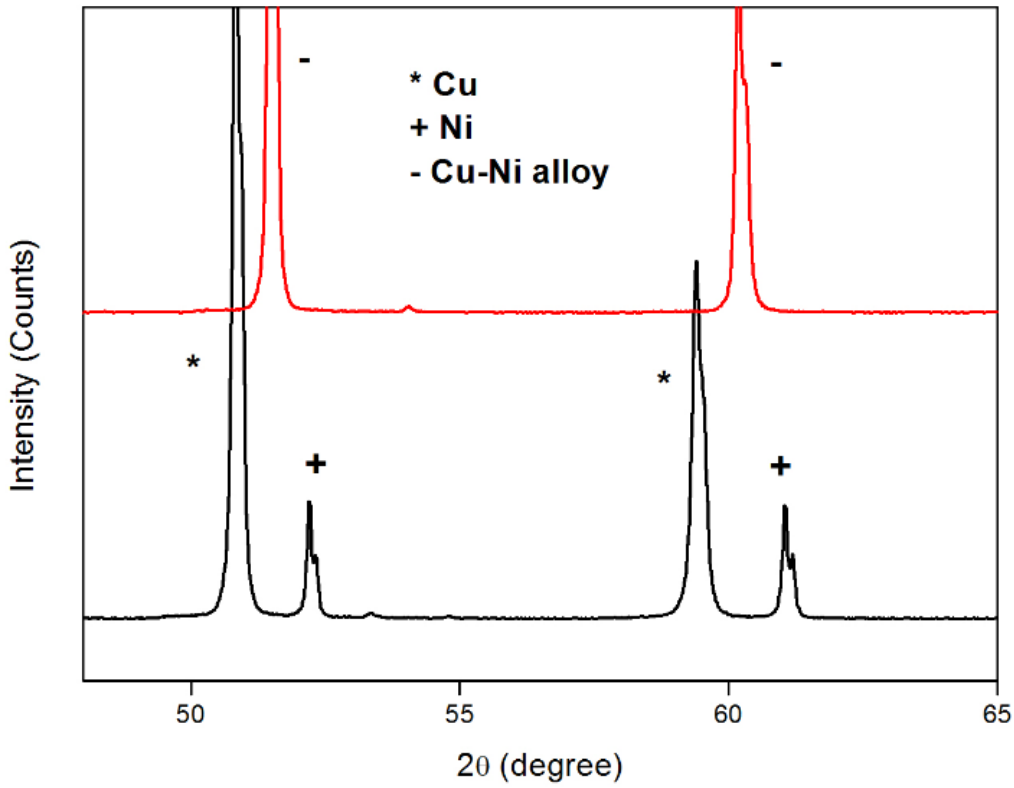

Figure 5.3. XRD patterns of copper coated nickel foil (Cu/Ni weight ratio =0.4): (a) before and (b) after heating at 750^{o}C in 5% H_2 balanced with N_2 for 20 h.

5.3.2. Carbon deposition from syngas on copper coated nickel

The carbon deposition weights from syngas on uncoated and copper coated nickel foils with different Cu/Ni ratios are shown in Fig. 5.4. After exposure to syngas at 750^{o}C for 20 h the weight gain on uncoated nickel foil was 52 wt%. However, the carbon deposition weight gain decreased with increasing amount of copper coating. There was no obvious carbon deposition when the weight ratio of Cu/Ni was greater than 0.4.

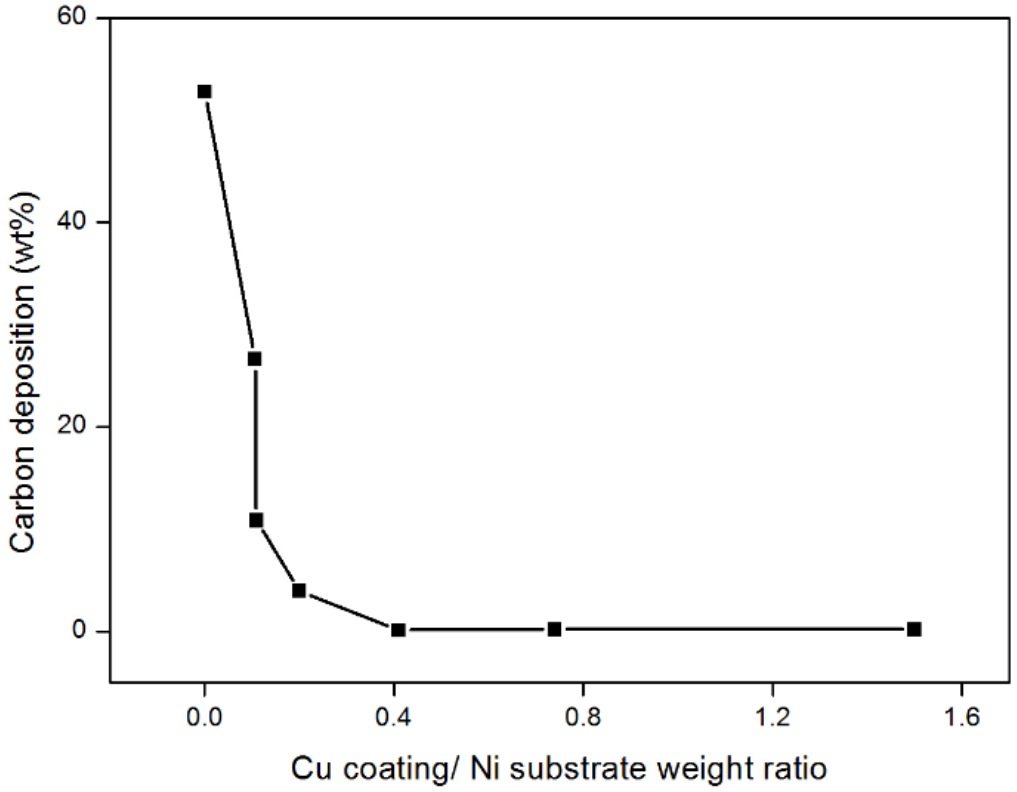

Figure 5.4. The effects of syngas on uncoated and copper coated nickel foil.

Fig. 5.5 compares SEM images of uncoated and copper coated nickel foil after exposure to syngas at 750°C for 20 h. Carbon in the form of black powder was deposited onto the surfaces of nickel foil or foam samples. These data confirmed the findings of other authors [3]. In contrast to the uncoated nickel samples, there were no detectable carbon deposits on copper coated nickel samples having higher copper content (Cu/Ni > 0.4) after heating in syngas, and these samples retained their copper-nickel alloy color. SEM images (Fig. 5.5) revealed carbon deposits on the uncoated nickel foil, which was confirmed as graphite by XRD analysis (Fig. 5.6).

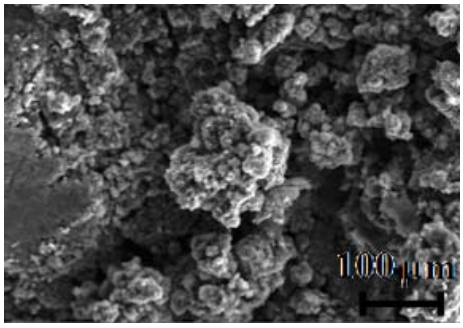

(a) Nickel foil exposed to syngas

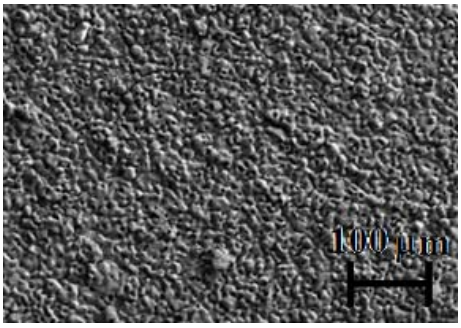

(b) Coated nickel foil with Cu/Ni = 0.4 exposed to syngas

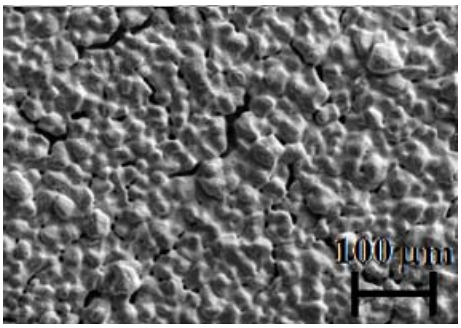

(c) Coated nickel foil with Cu/Ni = 0.7 exposed to syngas

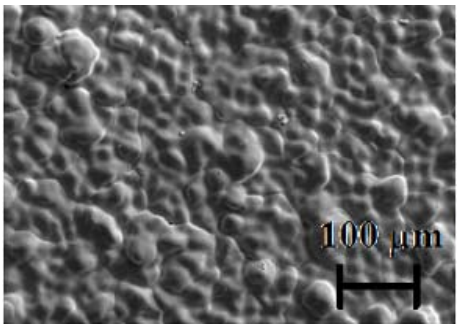

(d) Coated nickel foil with Cu/Ni = 1.5 exposed to syngas

Figure 5.5. SEM images of uncoated and copper coated nickel foil samples exposed to syngas for 20 h at 750 ^{o}C.

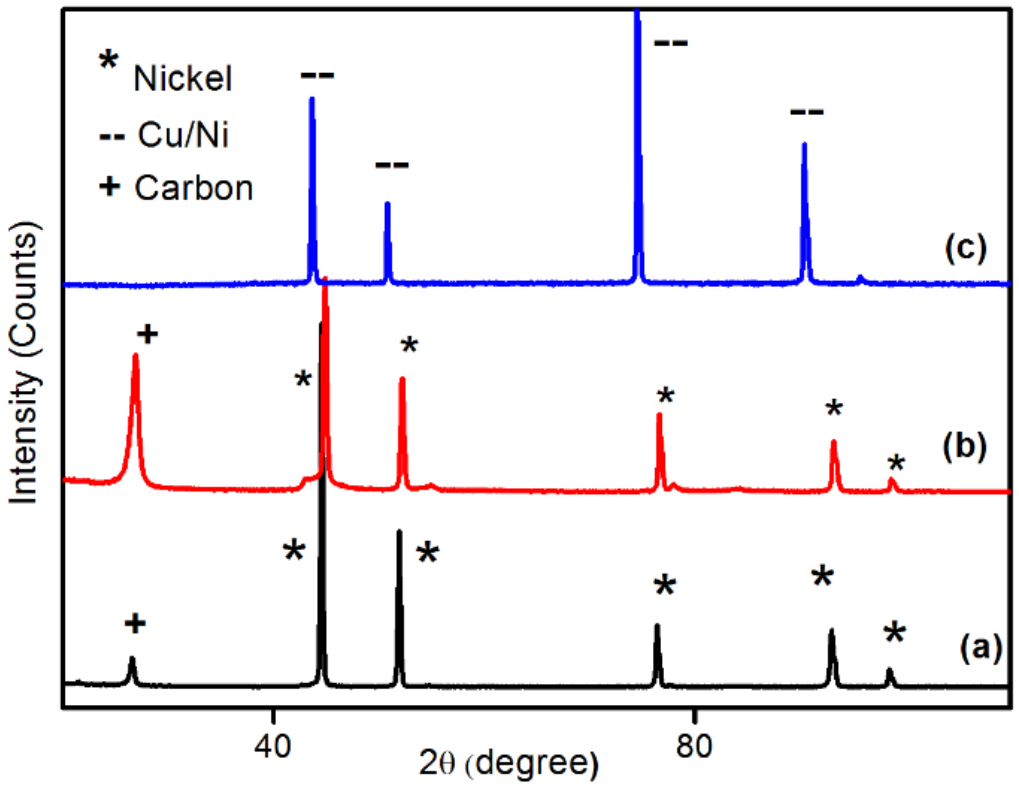

Figure 5.6. XRD patterns of: (a) nickel foam; (b) nickel foil; and (c) copper coated nickel foil (Cu/Ni = 0.4), after exposure to syngas at 750 ^{o}C for 20 h.

Carbon deposition on nickel in the presence of carbon monoxide is a well known phenomenon. It has been shown that carbon deposition on nickel-based anodes blocks the active sites and thus decreases fuel cell performance [4 - 6]. The mechanism of carbon deposition on metal is complex [5, 7, 8]. Initially, the carbon bearing gases are absorbed on the metal surface, followed by the formation of carbon through the following reactions [4, 6, 7, 9-12]:

$$2CO_{(g)} \rightarrow CO_{2(g)} + C_{(s)} \quad (5.3)$$

$$CO_{(g)} + H_{2(g)} \rightarrow H_2O_{(g)} + C_{(s)} \quad (5.4)$$

Carbon is deposited on the surface of nickel as black filaments. Hydrogen present in syngas causes weakening of grain boundaries in nickel by diffusing into

the metal. The deposited carbon is transferred into the nickel phase. Since the solubility of carbon in nickel is low, nickel easily became oversaturated with carbon and was followed by graphitization which caused total disintegration of the nickel into particles. The metastable nickel carbide Ni_3C was not accumulated but directly decomposed into nickel particles and carbon [4], hence no Ni_3C was detectable using XRD (Fig. 5.6), attributed to its decomposition at high temperatures [1,7, 13, 14]. The nickel particles act as catalyst sites for further carbon deposition.

In contrast to nickel, copper shows no catalytic activity for decomposition of CO [4]. Carbon deposition can be suppressed by alloying nickel with more than 20 wt% of copper [15]. A new model explaining the carbon free surface for copper-nickel alloy has been developed [16-17]. The nickel metal destruction processes (formation and thermal decomposition of nickel carbides) cannot propagate deep into copper-nickel alloy due to the shielding effect of copper and the copper-nickel alloy. Hence there is no major reconstruction of the copper-nickel alloy due to the absence of formation of bulk carbide.

5.3.3. Stability of copper coated nickel in H_2S-containing atmosphere

Fig. 5.7 compares the weight changes of copper coated nickel with different Cu/Ni ratios exposed to 500 ppm H_2S balanced with N_2 or syngas at 750 ^oC for 20 h. The weight gains in 500 ppm H_2S-containing N_2 were larger than those in 500 ppm H_2S-containing syngas for the corresponding copper coated nickel with the same ratio of Cu/Ni. As the Cu/Ni ratio was increased from 0 to 1.5, the weight gain decreased from 2.3% to 0.5% in 500 ppm H_2S balanced with N_2 at 750 ^oC for

20 h. However, the amount of weight gain in H_2S-containing syngas was not obviously dependent on Cu/Ni ratio and generally less than 0.35 wt%. It should be noted that the complexity of reactions on the metal surface in the H_2S-syngas mix does not allow unequivocal evaluation of stability simply through use of weight changes. When nickel is exposed to H_2S-syngas, weight gained might occur due to the formation of nickel sulfide and carbon deposition; weight loss might occur due to the total disintegration of nickel.

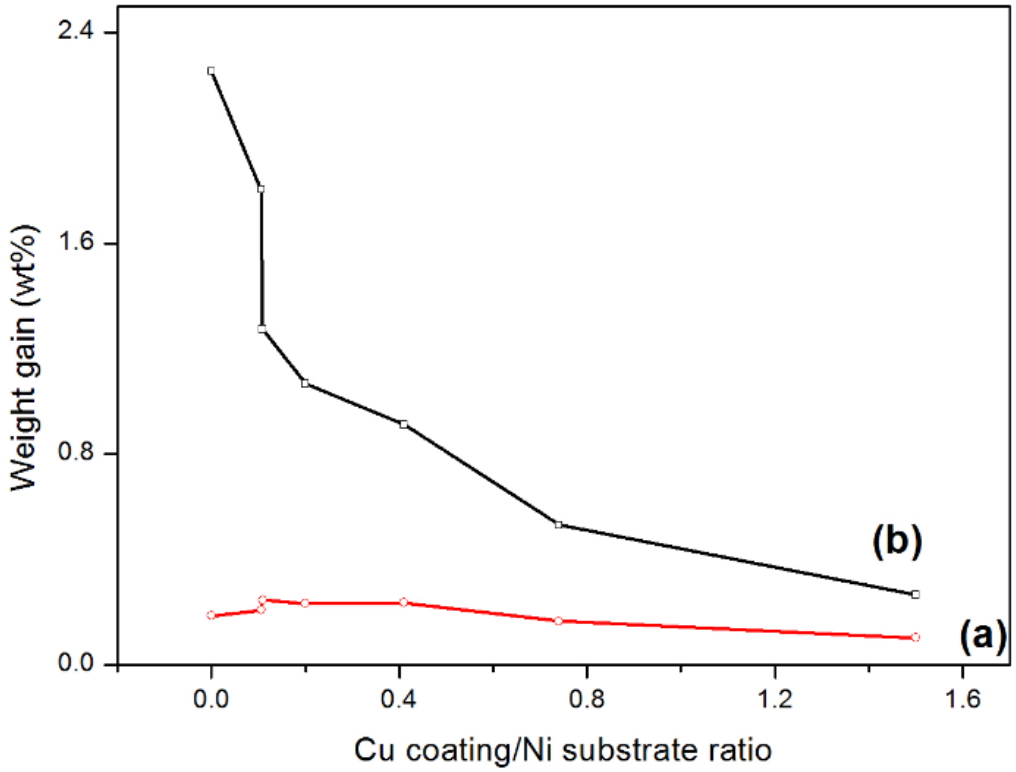

Figure 5.7. The weight gain versus Cu/Ni weight ratio after exposure to: (a) 500 ppm H_2S-syngas; and (b) 500 ppm H_2S-N_2 at 750^{o}C for 20 hours.

Thermodynamically, H_2S can react with either nickel or copper to form sulfides (weight gain) through the following reactions:

$$Cu + H_2S \leftrightarrow CuS + H_2 \qquad (5.7)$$

$$Ni + H_2S \leftrightarrow NiS + H_2 \quad (5.8)$$

The calculated Gibbs free energies of the above reactions are shown in Fig. 8. Both reactions are thermodynamically less favorable at higher temperatures, though copper has a lower tendency to form sulfides. When copper and nickel form an alloy the tendency to form individual nickel and copper sulfides is reduced. In addition, as indicated in Equations (5.7) and (5.8), hydrogen is a product of the corroding reactions. High partial hydrogen pressure in syngas will drive the reaction towards the left and thereby reduce the formation of sulfides. In our experiments metal sulfides were more easily formed in 500 ppm H_2S - N_2 than in 500 ppm H_2S - syngas containing about 40% hydrogen. For nickel foil exposed to 500 ppm H_2S-N_2, XRD (Fig. 5.9) confirmed the formation of Ni_3S_2. There are no detectable amounts of copper sulfide after exposure to 500 ppm H_2S-syngas.

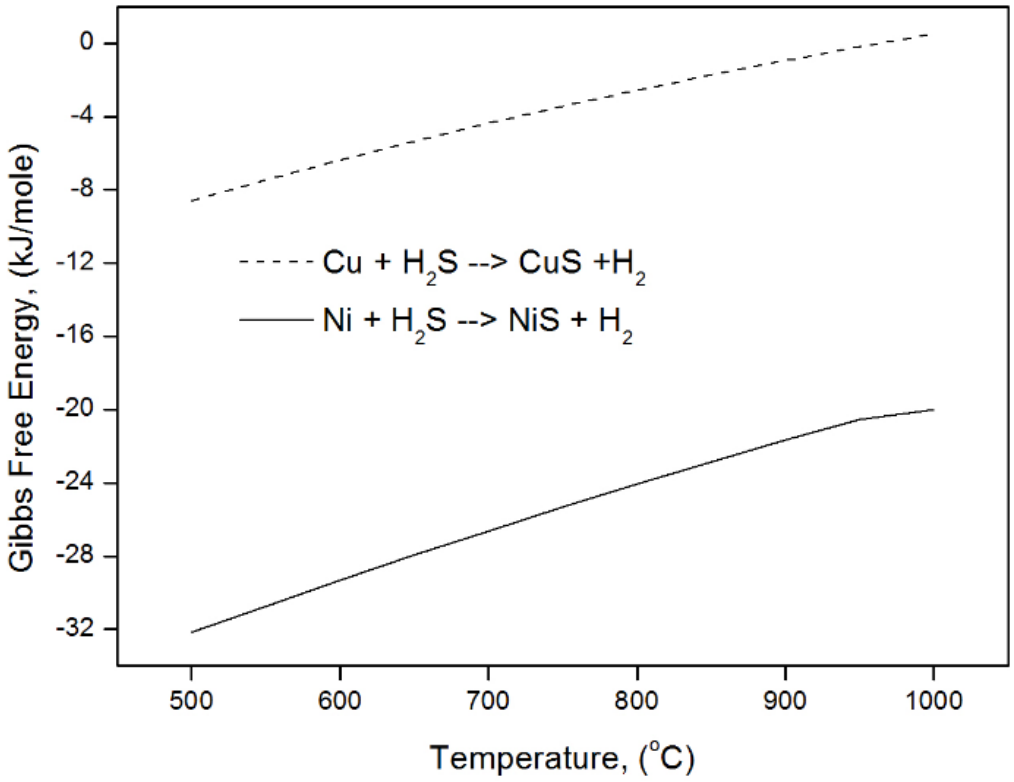

Figure 5.8. Gibbs free energy as a function of temperature for reactions of individual nickel and copper with hydrogen sulfide.

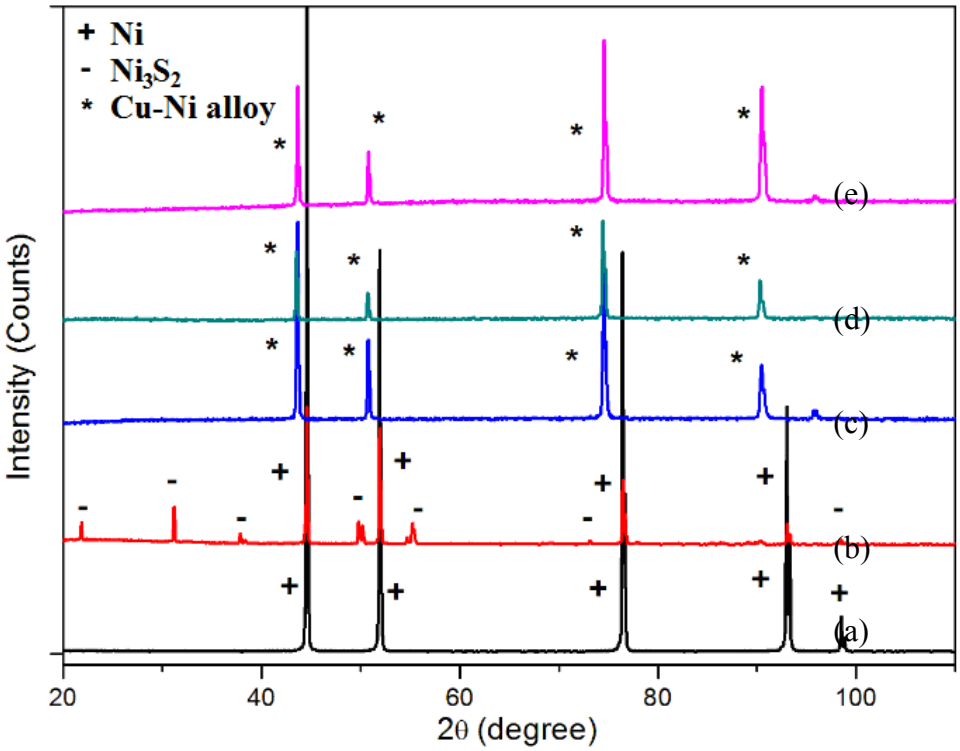

Figure 5.9. XRD patterns of copper coated or plain nickel foil samples exposed in different atmospheres for 20 h at 750°C: (a) nickel foil in 5% H_2-N_2; (b) nickel foil in 500 ppm H_2S-N_2; (c) copper coated nickel foil (Cu/Ni weight ratio =0.74) in 5% H_2-N_2; (d) copper coated nickel foil (Cu/Ni weight ratio=0.74) in 500ppm H_2S-N_2; (e) copper coated nickel foil (Cu/Ni weight ratio =0.74) in 500 ppm H_2S-syngas.

5.4. Conclusions

Copper coated nickel foam exhibited strong resistance to carbon deposition and sulfidizing in carbon or/and sulfur containing gas at elevated temperature. In contrast, uncoated nickel foam suffered severe cracking and loss of mechanical strength after exposure to H_2S-containing syngas. Based on the current work, copper coated nickel foam has significant potential value for use as current collector for solid oxide fuel cells fed by H_2S-containing syngas.

5.5. References

1. X.Z. Fu, J. Melnik, Q.X. Low, J.L. Luo, K.T. Chuang, A.R. Sanger and Q.-M. Yang, Int. J. Hydrogen Energy. 35 (2010) 11180.

2. J.W. Dini, Electrodeposition: The Materials Science of Coatings and Substrates, Noyes Publications, New Jersey, 1993.

3. X.F. Ye, S.R. Wang, J. Zhou, F.R. Zeng, H.W. Nie and T.L. Wen, J. Power Sources. 195 (2010) 7264.

4. A.I. La Cava, C.A. Bernardo and D.L. Trimm, Carbon. 20 (1982) 219.

5. Y. Sone, H. Kishida, M. Kobayashi and T. Watanabe, J. Power Sources. 86 (2000) 334.

6. C.A. Bernardo, I. Alstrup and J.R. Rostrup-Nielsen, J. Catal. 96 (1985) 517.

7. A. Sacco, P. Thacker, T.N. Chang and A.T.S. Chiang, J. Catal. 85 (1984) 224.

8. R.T.K. Baker, M.A. Barber, P.S. Harris, F.S. Feates and R.J. Waite, J. Catal., 26, 51 (1972).

9. H.J. Grabke, Mater. Corros., 54 (2003) 736.

10. R.F. Hochman and J.H. Burson, in API Division of Refining Proceedings, 1966, 331.

11. D. Bianchi and C.O. Bennett, J. Catal. 86 (1984) 433.

12. J. Rostrup-Nielsen and D.L. Trimm, J. Catal. 48 (1977) 155.

13. P.L. Walker, J.F. Rakszawski and G.R. Imperial, J. Phys. Chem. 63 (1959) 133.

14. N. A. Jarrah, F. Li, J. G. Van Ommen and L. Lefferts, J. Mater. Chem. 15 (2005) 1946.

15. J. Zhang, D.M.I. Cole and D.J. Young, Mater. Corros. 56 (2005) 756.

16. M. Duchamp, J.D. Bartout, S. Forest, Y. Bienvenu, G. Walther, S. Saberi and A. Boehm, IUTAM Symposium on Mechanical Properties of Cellular Materials, Springer Netherlands, 2009, 51.

17. U. Köhler, C. Antonius and P. Bäuerlein, J. Power Sources. 127 (2004) 45.

18. H.J. Grabke, CORROSION. 51 (1995) 711.

19. H.J. Grabke, Mater. Corros. 49 (1998) 303.

20. H.J. Grabke, R. Krajak and E.M. Müller-Lorenz, Mater. Corros. 44 (1993) 89.

21. R.P. O'Hayre, S.-W. Cha, F.B. Prinz and W. Colella, Fuel cell fundamentals, John Wiley & Sons, New Jersey, 2006.

22. J. Fergus, R. Hui, X. Li, D.P. Wilkinson and J. Zhang, Solid Oxide Fuel Cells: Materials Properties and Performance, CRC Press, Florida, 2009.

23. H.J. Grabke, M. Schütze and M. Tze, Corrosion by Carbon and Nitrogen - Metal Dusting, Carburisation and Nitridation (EFC 41), in, Woodhead Publishing, 2007.

24. C.A. Bernardo, I. Alstrup and J.R. Rostrup-Nielsen, J. Catal. 96 (1985) 517.

25. Y. Nishiyama, K. Moriguchi, N. Otsuka and T. Kudo, Mater. Corros. 56 (2005) 806.

26. D.J. Young, J. Zhang, C. Geers and M. Schütze, Mater. Corros. 62 (2010) 7-28.

27. J. Klöwer, H.J. Grabke and E.M. Müller-Lorenz, Mater. Corros. 49 (1998) 328.

38. E.W. Park, H. Moon, M.-S. Park and S.H. Hyun, Int. J. Hydrogen Energy. 34 (2009) 5537.

29. Y. Nishiyama and Y. Tamai, J. Catal. 33 (1974) 98.

30. Y. Nishiyama and Y. Tamai, J. Catal. 45 (1976) 1.

31. I. Alstrup, J. Catal. 109 (1988) 241.

32. J. Zhang, D.M.I. Cole and D.J. Young, Mater. Corros. 56 (2005) 756.

33. H. He, R.J. Gorte and J.M. Vohs, Electrochem. Solid-State Lett. 8 (2005) A279.

34. M. Gong, X. Liu, J. Trembly and C. Johnson, J. Power Sources. 168 (2007) 289.

35. Y. Matsuzaki and I. Yasuda, Solid State Ionics. 132 (2000) 261.

6.0. Comparison of stability and electrical resistivity of copper coated and copper-ceria coated nickel foams as current collectors for solid oxide fuel cells operating with H_2S-containing syngas as fuel*

6. 1. Introduction

This section we compared the performance of nickel foam having either of two types of protective coatings, each of which has excellent electronic conductivity and good resistance to both sulfur corrosion and carbon deposition: copper coated nickel foam and copper-ceria coated nickel foam.

6.2. Experimental

6.2.1. Sample preparation

Two electrodeposition techniques were used to fabricate copper coated and copper-ceria coated nickel foam: electrodeposition from a solution containing copper ions and co-electrodeposition from a solution containing copper ions and ceria nanoparticles. The compositions of the ion solution/suspension are shown in Table 6.1. The same plating condition, methods and samples characterization described in section 5.2.1 was used in this section.

** A version of this chapter will be submitted to Applied Surface Science for publication.*

Table 6.1. Plating parameters used for electrodeposition and co-electrodeposition.

Parameters	Electrodeposition Cu coated Ni	co-electrodeposition Cu-CeO_2 coated Ni
Copper(II) sulfate $CuSO_4 \cdot xH_2O$	180 g/L	
Sulfuric acid (H_2SO_4)	60 g/L	
CeO_2 nanoparticles	N/A	200 g/L
Anode	Cu, 30 mm × 60 mm	
Cathode	nickel foam	
Current density	10 mA/cm^2	80 mA/cm^2
Average deposition area	7.14 cm^2	
Deposition time	8 h	1 h

6.2.2. Van der Pauw 4 point stability measurement and samples characterization

The Van der Pauw 4-points conductivity measurement method was used to test the stability of coated nickel foam under different atmospheres at 750^{o}C for at least 40 h. Properties of copper coated and copper-ceria coated nickel foams were compared using 500 ppm H_2S balance N_2. H_2S-containing syngas (500 ppm H_2S, 40 % H_2, balance CO) was used to determine the long term stability of the electrical conductivity of uncoated and coated nickel foams using a ProbeStat^{TM} (NorECs Company) instrument. Gold wire was used as the 4-points contacts and for connection to the ProbeStat^{TM} base unit. The device was placed into a quartz tube and then heated in 5% H_2-N_2. After the system was stable for at least 1 h at

750^{o}C, 500 ppm H_2S-N_2 or 500 ppm H_2S-containing syngas was introduced at a flow rate of 50 cm^3/min and the resistance of the samples was determined as a function of time. Nitrogen gas at a flow rate of 50 cm^3/min was used to protect the sample after the tests as the system cooled down to room temperature (cooling rate 3^{o}C/min).

6.3. Results and discussion

6.3.1. Characterization of copper coated and copper-ceria coated nickel foams

For the samples' stability tests, a deposition time of 8 h was used to deposit copper and copper-ceria onto nickel foam with Cu/Ni weight ratio 2.5. The corresponding current densities for copper coating and copper-ceria coating were 10 mA/cm^3 and 80 mA/cm^3. A higher current density was required for copper-ceria coating because a high concentration of CeO_2 nanoparticles was used with the consequence that the deposition efficiency was reduced. . The ceria was detected in the copper coating and this coating formed copper-nickel alloy after heat treatment (Fig. 6.1).

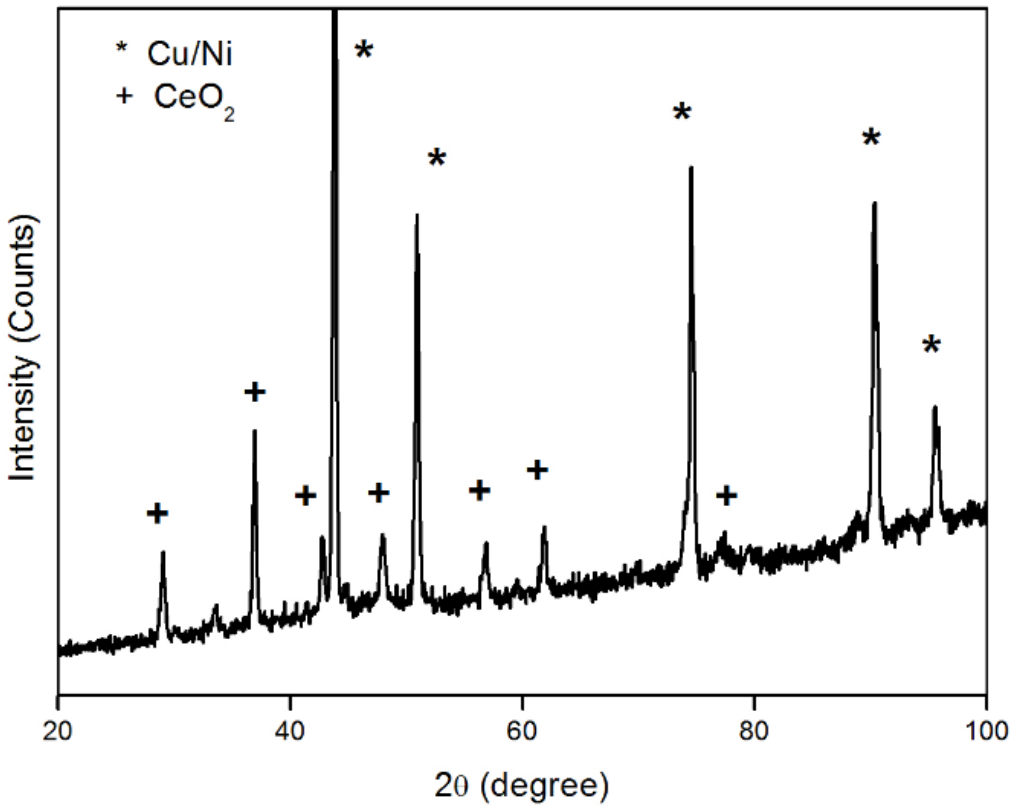

Figure 6.1. The XRD pattern for copper-ceria coated nickel foam after 900°C heat treatment in reducing atmosphere for 20 h.

6.3.2. Comparison of copper coated and copper-ceria coated nickel foam in H_2S-N_2

The chemical stabilities of copper coated and copper-ceria coated nickel foam in the absence of CO were compared using 500 ppm H_2S-N_2 at 750°C using Van der Pauw 4-points conductivity method (Fig. 6.2). The resistivity of copper coated nickel foam increased immediately on exposure to H_2S, but the resistivity of copper-ceria coated nickel foam was more stable during five hours exposure to H_2S. The rate of increase in resistance was faster for copper coated nickel foam than for copper-ceria coated nickel foam. The primary role of ceria in reforming applications is as oxidation catalyst for hydrocarbons (e.g.natural gas) [1].

However, when using ceria together with copper as current collector in H_2S fuel cells, H_2S reacts with ceria to replace lattice oxygen with sulfur [2-5]. For copper coated nickel foam in H_2S-N_2, reaction of metals and hydrogen sulfide was rapid, forming metal sulfides which increased the resistance of copper coated nickel foam. However, the ceria component of copper-ceria coated nickel foam served as a absorbent and significantly reduced the metal-H_2S rate of reaction. However, when exposed to H_2S for an extended period the outer layer of ceria became exhausted, followed by attack on the copper to form copper sulfides (Cu_2S), thus increasing the resistance of the coating. The H_2S continued to corrode the inner part of the copper-ceria coating. The ceria in the inner layer of the coating continued to resist H_2S attack, thus reducing the rate of increase in resistance when compared to copper coated nickel foam. The XRD patterns of copper coated and copper-ceria coated nickel foam (Fig. 6.3) showed the formation of metal sulfide and cerium copper oxide sulfide ($CeCu_{0.987}OS$).

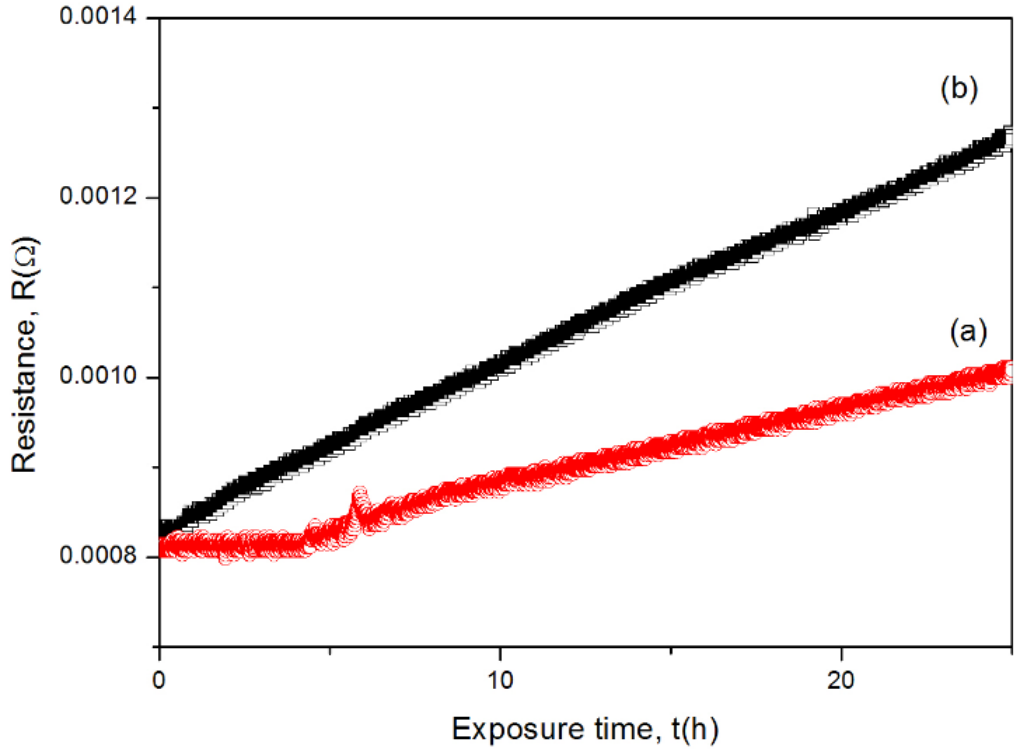

Figure 6.2. Comparison of the stability of the resistivities of (a) copper-ceria coated and (b) copper coated nickel foam under 500 ppm H_2S-N_2 at 750°C.

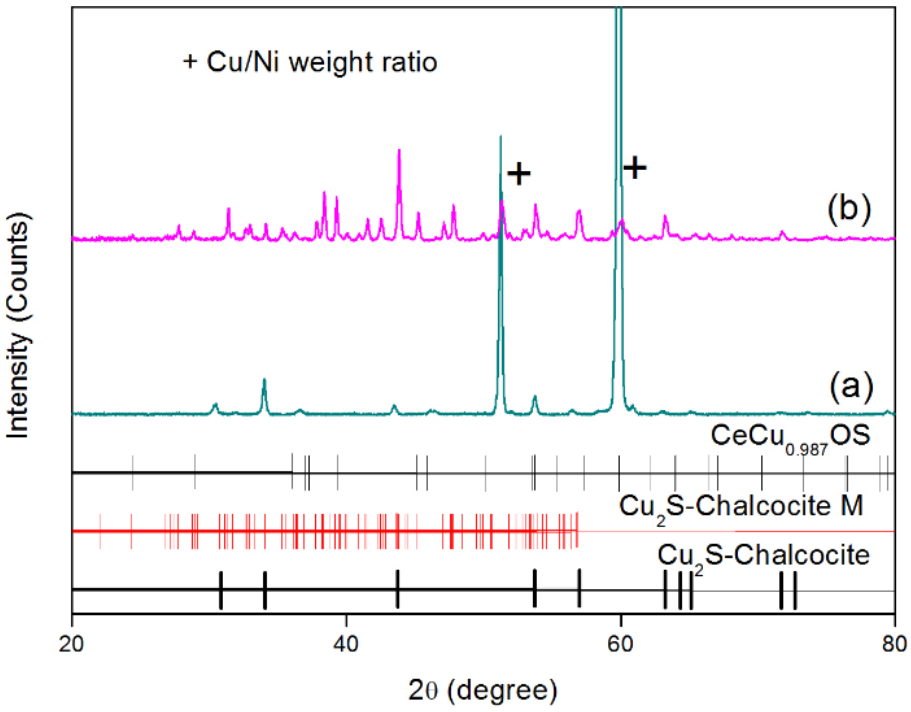

Figure 6.3. The XRD patterns for (a) copper coated and (b) copper-ceria coated nickel foam after exposure to 500 H_2S-N_2 at 750^oC for 40 h.

6.3.3. Comparison of stabilities of uncoated and coated nickel foam in syngas and H_2S-syngas

The long-term electronic resistance stabilities of uncoated and copper/copper-ceria coated nickel foams under different atmospheres were compared using the Van der Pauw 4-point method (Fig. 6.4). The samples were exposed to different atmospheres for at least 40 h. The resistance of nickel foam increased 132-fold after exposure to syngas. The carbon (graphite filamentous) deposited (identified using XRD, Fig. 6.5) on the nickel foam not only increased the resistance but also led to destruction of the nickel foam. The SEM images (Fig. 6.6 c and 6.6 d) show there was significant deposition of carbon on uncoated nickel foam and the particles agglomerated into grains < 1 μm. The destruction of the nickel structure after 40 h exposure was accompanied by a sudden increase in resistance (Fig. 6.4 b). The destruction of the nickel structure caused separation of the nickel foam from the electrode, with a concomitant sudden increase in total resistance.

After nickel foam was exposed to H_2S-syngas no carbon was detected by XRD (Fig. 6.5). The H_2S in the syngas poisoned the carbon deposition sites of the nickel foam thus inhibiting the carbon deposition process. The SEM images (Fig. 6.6 e and Fig. 6.6 f) showed no carbon formation, but there was some destruction of the structure of the nickel foam after exposure to H_2S-syngas. H_2S poisoned the surface of nickel foam by forming Ni_xS. After exposure to H_2S-syngas for a long

period of time, some “weak spots” which were not completely covered by sulfur and carbon deposition started to form below the sulfur layer (Fig. 6.7) [6, 7-11]. Although the amount of deposited carbon was too small to be detected by XRD, the structure of nickel was partly destroyed.

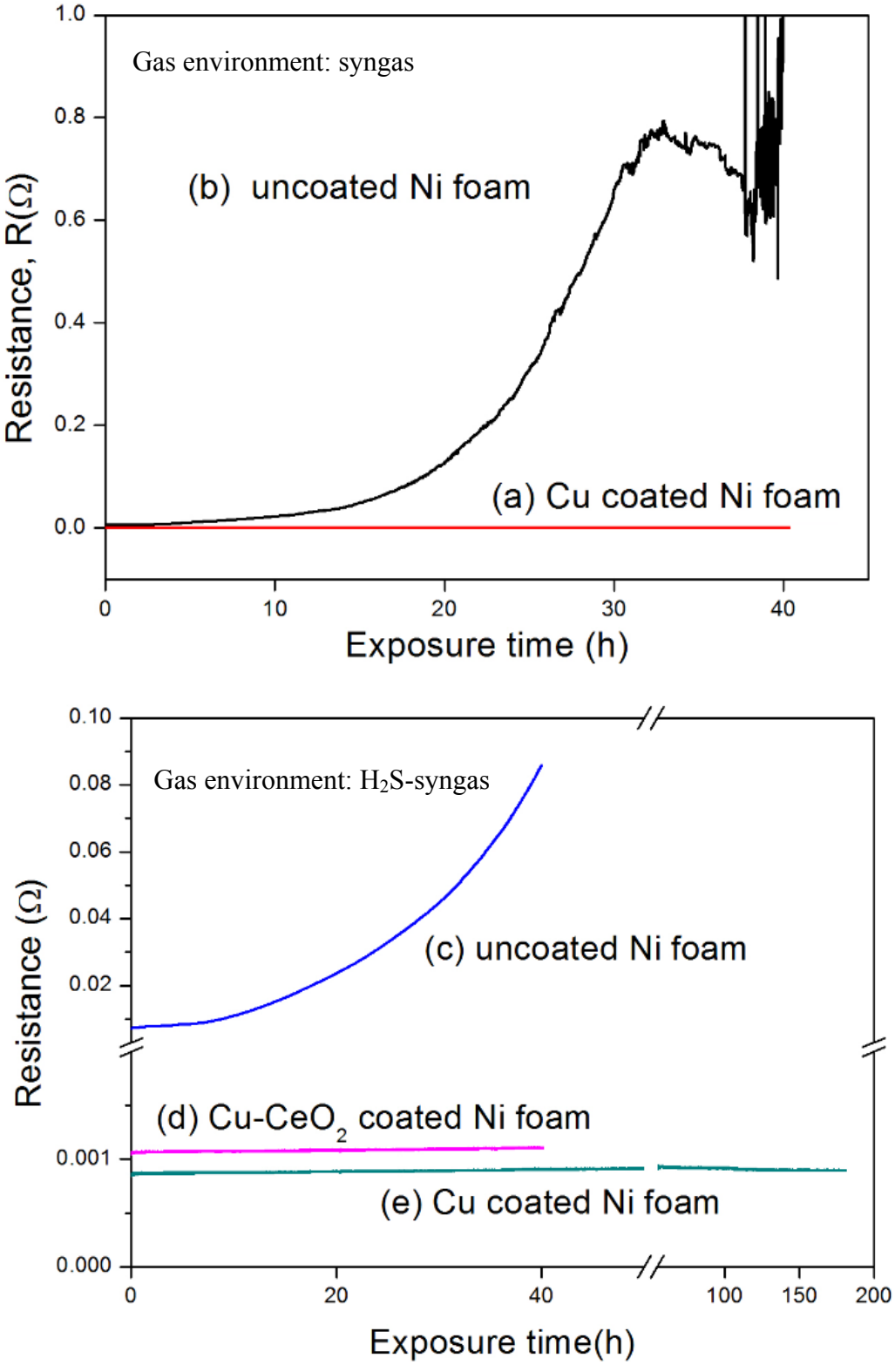

Figure 6.4. Comparison of resistances of uncoated and coated nickel foams.

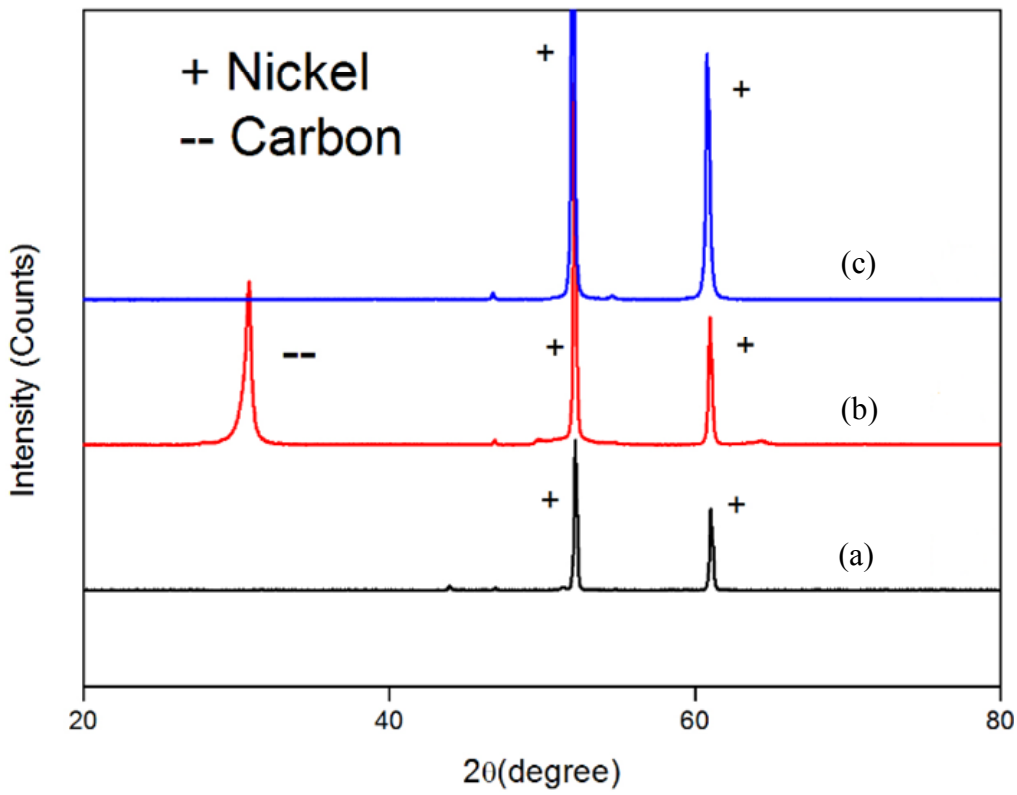

Figure 6.5. The XRD patterns of nickel foam after exposure to: (a) 5% H_2-N_2; (b) syngas; and (c) 500 ppm H_2S-syngas at 750^oC.

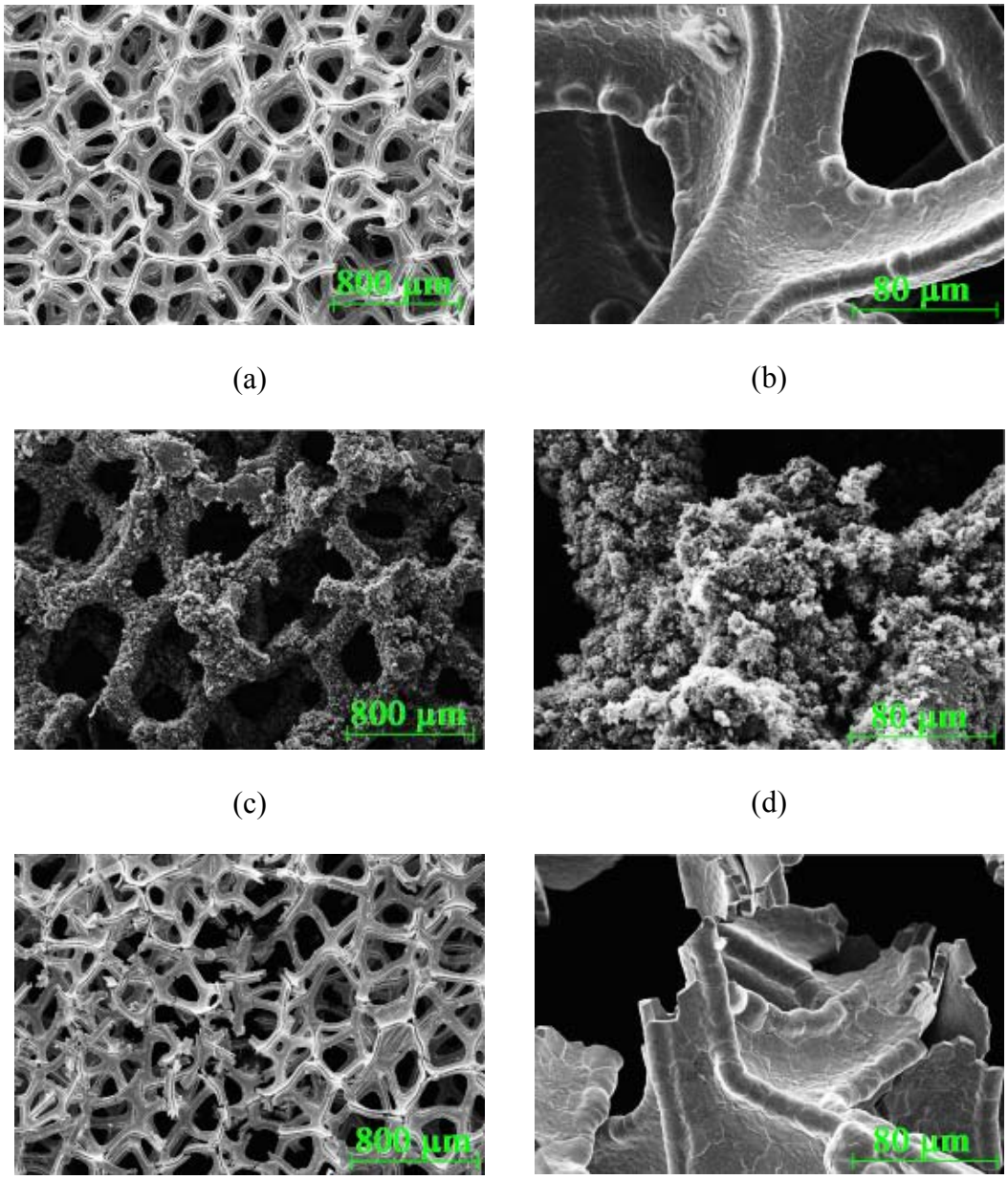

Figure 6.6. SEM images of nickel foam at different magnifications after exposure to (a and b) 5 % H_2; (c and d) syngas; (e and f) 500 ppm H_2S-syngas.

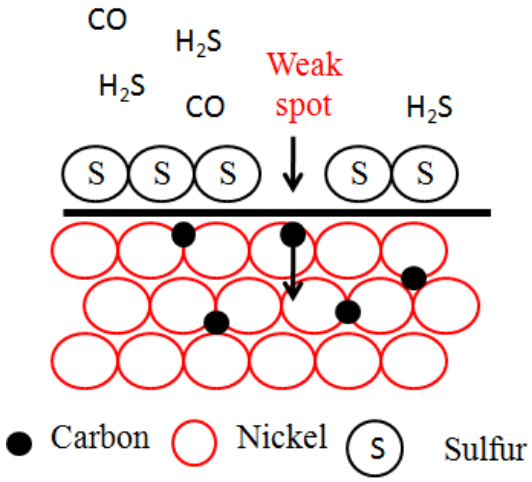

Figure 6.7. Schematic representation of attack of H_2S-syngas on nickel.

In contrast, copper coated nickel foam exposed to syngas showed very stable, low electronic resistance (Fig. 6.4 b) and excellent mechanical strength during more than 40 h in syngas. Experiments were conducted in solid oxide fuel cells using copper coated nickel foam as the anode current collector, anode LSCM catalyst, YSZ electrolyte, porous Pt cathode, and syngas as fuel. This fuel cell setup with copper coated nickel foam anode current collector provided similar power density and excellent stability at 900^{o}C when compared to cells having gold anode current collectors [15]. The XRD pattern (Fig 6.9) and SEM images (Fig. 6.8 c and Fig. 6.8 d) confirmed that there was no carbon formation.

Copper coated nickel foam showed very stable resistance (Fig. 6.4 e) during exposure to H_2S-syngas. The copper-ceria coated nickel foam exposed to H_2S-syngas also showed stable resistance (Fig. 6.4 d). There was no formation of copper sulfide by copper coated and copper-ceria coated nickel foam (Fig. 6.9). The copper-ceria coated nickel foam reacted with H_2S and formed $CeCu_{0.987}OS$. Cracks formed in copper-ceria coating after heating in reducing atmosphere and

so a contiguous, dense coating could not be obtained (Fig. 6.10). Although copper-ceria coated nickel foam showed better performance in H_2S-N_2, the formation of cracks makes it unsuitable for use as current collector.

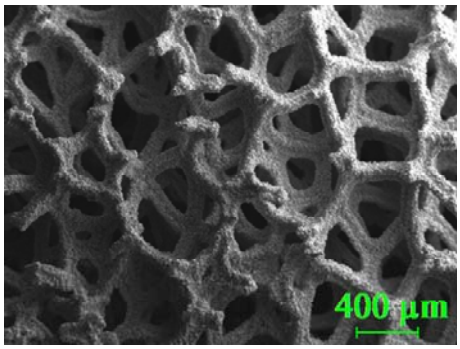

(a) Gas environment: 5% H_2-N_2

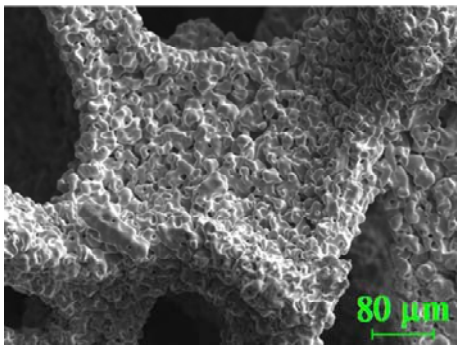

(b) Gas environment: 5% H_2-N_2

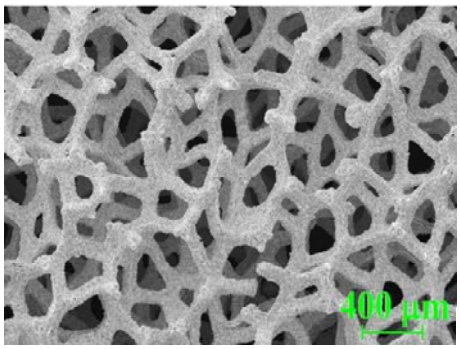

(c) Gas environment: Syngas

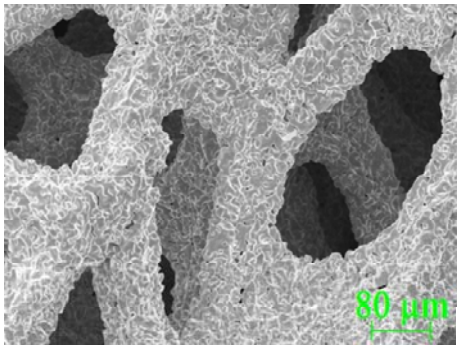

(d) Gas environment: Syngas

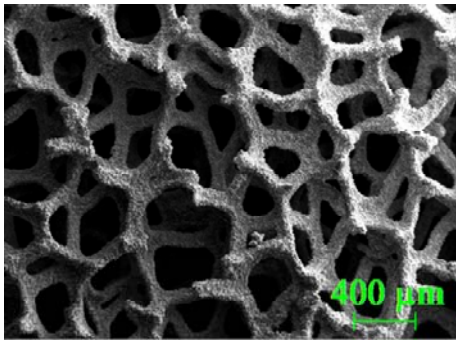

(e) Gas environment: H_2S-Syngas

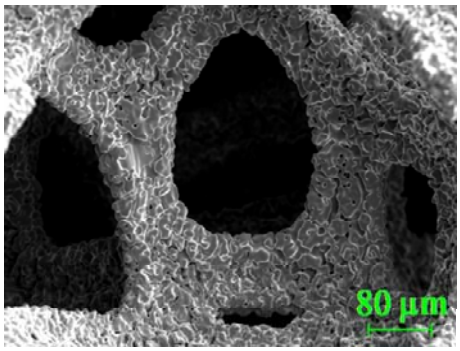

(f) Gas environment: H_2S-Syngas

Figure 6.8. SEM images of copper coated nickel foams (Cu/Ni weight ratio = 0.25) exposed to different gas atmosphere at 750^{o}C.

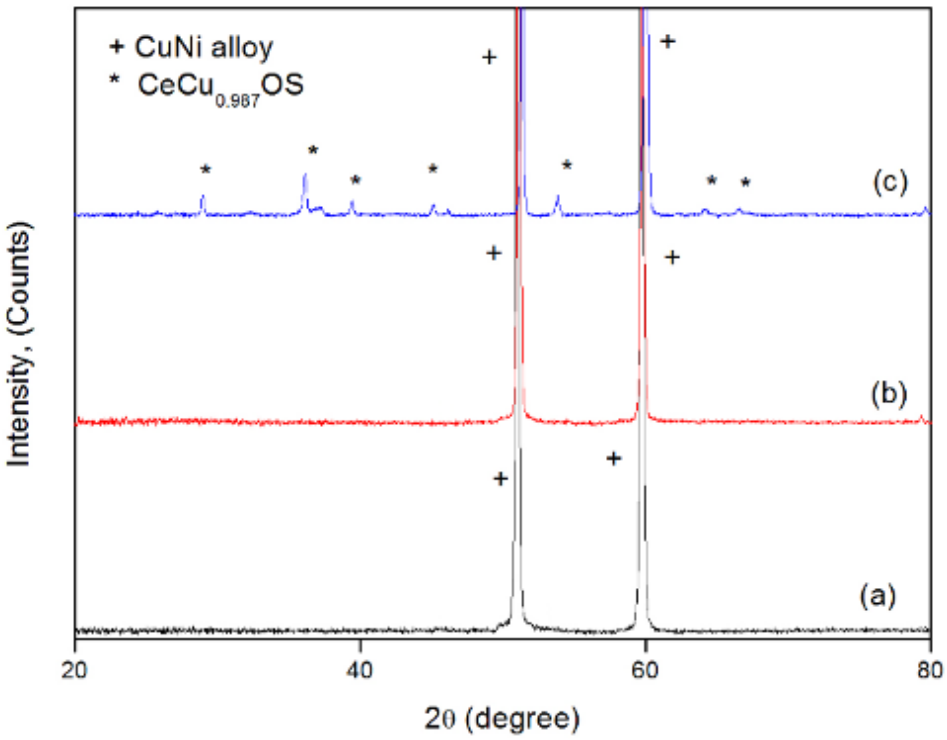

Figure 6.9. The XRD patterns of: (a) copper coated nickel foam exposed to syngas; (b) copper coated nickel foam exposed to 500 ppm H_2S-syngas; (c) copper-ceria coated nickel foam exposed to 500 ppm H_2S-syngas.

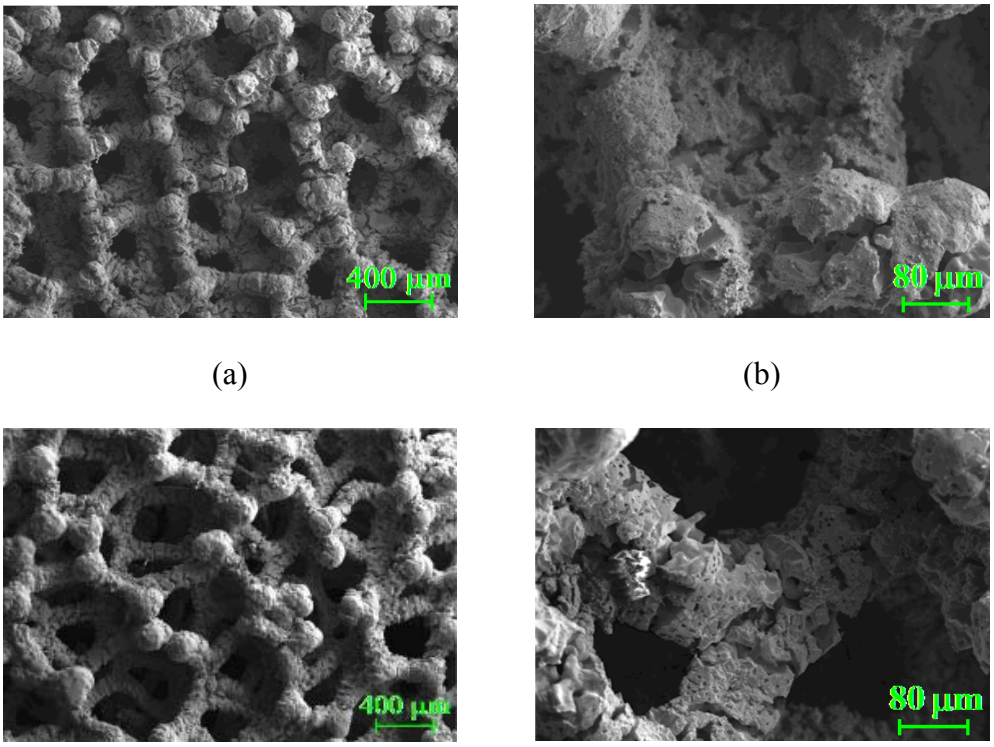

Figure 6.10. SEM images of copper-ceria coated nickel foam after exposure to: (a and b) 5 % H_2; (c and d) 500 ppm H_2S-syngas for 40 h.

6.4. Conclusions

Electrodeposition and co-electrodeposition are easy and effective techniques to form a copper based protective coating on nickel foam. Copper and copper-ceria successfully are coated onto nickel foam. Both of the coatings form a copper-nickel alloy during heat treatment in reducing atmosphere. Copper coated and copper-ceria coated nickel foams have low, stable resistance during extended exposure to H_2S-syngas at 750^oC. The resistance of copper-ceria coated nickel foam increases slowly compared to copper coated nickel foam in H_2S-N_2 at 750^oC. The ceria acts as absorbent to H_2S, thereby decreasing the rate of metal sulfidation. After exposure to either syngas or sour syngas, bare nickel becomes severely

cracked, causing loss of mechanical strength and a concomitant large increase in resistance. In contrast, copper coated and copper-ceria coated nickel foams are highly resistant to both carbon deposition and sulfur corrosion. Although copper-ceria coating has better stability compared to copper coating, cracks are formed and a contiguous dense layer of coating cannot be obtained through high temperature heating, thus making this material unsuitable to use as anode current collector in SOFC applications.

6.5. References

1. J. P. Trembly, A. I. Marquez, T. R. Ohrn and D. J. Bayless, *Journal of Power Sources*, **158**, 263 (2006).

2. S. M. Haile, *Acta Materialia*, **51**, 5981 (2003).

3. Z. Xie, C. Xia, M. Zhang, W. Zhu and H. Wang, *Journal of Power Sources*, **161**, 1056 (2006).

4. H. D. Joubert, J. J. Terblans and H. C. Swart, *Nuclear Instruments and Methods in Physics Research Section B: Beam Interactions with Materials and Atoms*, **267**, 2575 (2009).

5. J. W.Dini, *Electrodeposition The Materials Science of Coatings and Substrates*, Noyes Publications, New Jersey (1993).

6. M. Gong, X. Liu, J. Trembly and C. Johnson, *Journal of Power Sources*, **168**, 289 (2007).

7. H. J. Grabke, *CORROSION*, **51**, 711 (1995).

8. H. J. Grabke, *Materials and Corrosion*, **49**, 303 (1998).

9. H. J. Grabke, *Materials and Corrosion*, **54**, 736 (2003).

10. H. J. Grabke, R. Krajak and E. M. Müller-Lorenz, *Materials and Corrosion*, **44**, 89 (1993).

11. A. Schneider, H. Viefhaus, G. Inden, H. J. Grabke and E. M. Müller-Lorenz, *Materials and Corrosion*, **49**, 336 (1998).

12. U. Köhler, C. Antonius and P. Bäuerlein, *Journal of Power Sources*, **127**, 45 (2004).

13. I. Alstrup, *Journal of Catalysis*, **109**, 241 (1988).

14. Y. Nishiyama, K. Moriguchi, N. Otsuka and T. Kudo, *Materials and Corrosion*, **56**, 806 (2005).

15. Y. Nishiyama and Y. Tamai, *Journal of Catalysis*, **33**, 98 (1974).

7.0. Electrophoretic deposition of titania nanopowder onto nickel foam*

7.1. Introduction

Titanium dioxide (TiO_2) nanopowders with three different crystal structures including brookite, anatase and rutile offer a wide range of properties which can be fitted into different applications; including sensor catalysts, photocatalysis, solar cells, biomedical devices, corrosion and oxidation resistant coatings, etc[1-4]. In addition, it was shown that heat treatment of TiO_2 in reducing atmosphere converts it to Ti_4O_7 and Ti_5O_9 with higher electrical conductivity (300 $S \cdot cm^{-1}$) when compared to TiO_2 [5]. Also, excellent corrosion and oxidation resistance of this material make titanium dioxide a viable applicant for high temperature solid oxide fuel cells (SOFCs) current collectors [6].

There are several coating methods which have been used for applying ceramic coating for different applications, including chemical vapor deposition (CVD), dip coating, slurry and sol-gel infiltration, electrolytic deposition and electrophoretic deposition (EPD) [7-11]. Electrophoretic deposition (EPD) is economically interesting when compared to other expensive and complicated coating methods.

EPD is a colloidal processing method comprises two main processes including charging the particles in order to make a stable suspension and migrating these charged particles under electric field toward electrode with the opposite charge [12, 13]. Preparing an appropriate suspension with high level of stability and adjusted pH is a key factor in every colloidal process, particular EPD. In fact, the final properties of deposited layer including uniformity, attachment

** A version of this chapter will be submitted to Journal of European Ceramic society for publication.*

and porosity are dependent on the quality of the suspension. Electrostatic repulsion forces, and steric and electrosteric forces can be applied in order to stabilize particles in a suspension. Adjusting the pH of the suspension and/or using a dispersant are two different ways of charging the particles in aqueous or organic solvents [14, 15].

EPD has many advantages over other coating methods including simple setup, little constraint on the shape of substrate, precise control of the thickness by adjusting electric field, deposition time and particle loading [16]. This method enables uniform deposition of ceramics on substrates with complex shapes [14, 17-20].

Nickel foams are mass produced by depositing nickel onto a polymer foam and heating to a high temperature to remove the polymer substrates [21]. Nickel foam has a three dimensional structure which makes it suitable for many applications including filters, electrical screening, catalyst supporters, impact absorbent, etc [22-24]. High porosity, surface area and melting point, in addition to excellent electrical conductivity, make nickel foam a candidate for current collectors [25]. On the other hand, oxidation of nickel foam, carbon deposition and low resistance towards sulfur containing fuels limit the application of this material. Applying a protective layer on the nickel foam could be one of the solutions to extend its application.

Using EPD to coat nickel foam with a functional coating is a difficult process due to the complex shape of the foam structure. Many researchers have deposited ceramic coatings on metallic flat materials and fibers. However, few reports have

been using EPD on a metal foam.

This research will examine the effect of different parameters on the suspension stability and EPD of titanium dioxide nanopowders in order to find an optimum condition for coating nickel foam.

7.2. Experimental procedures

7.2.1. Materials

Anatase titanium oxide (TiO_2, Sigma Alrich, with particles size less than 25 nm, surface area of 200-220 m^2/g) was used as the ceramic powder for electrophoretic mobility measurement and electrophoretic deposition. Ethyl alcohol (anhydrous, Commercial Alcohol), triethanolamine (TEA, Sigma Alrich), poly(vinyl butral-co-vinyl) (PVB, average molecular weight 50000-80000, Sigma Aldrich) were used as solvent, dispersant and binder, respectively. The concentration of titanium oxide in the suspension was fixed at 2 wt% of suspension.

7.2.2. Suspension preparation

Titania (2 wt %) were added into ethanol containing different amount of TEA and PVB. The pH value of the solution was adjusted between 1 and 12 by adding HNO_3 (1.0 N, Sigma Aldrich) and NaOH (1.0 N, Fisher Scientific). After that, suspensions were sonicated using high energy ultrasonic probe (Sonics Vibra Cell) at amplitude of 30% and energy of 1000 kJ.

7.2.3. Electrophoretic mobility

An acoustic and electro-acoustic spectrometer (Model DT-1201) from Dispersion Technology Inc was used to measure the particle size distribution and

zeta potential of dispersed nanoparticles in prepared suspensions. All measurements were made at 20 ^{o}C. To ascertain the reliability, all measurements were repeated at least 5 times for each sample.

7.2.4. Substrates for electrophoretic deposition

Nickel foam (Vale Inco, porosity of 92%, average pore size of 0.6mm and a relative density of 7.8%.) was used as the substrates for electrophoretic deposition. The nickel foam was cleaned in acetone and ethyl alcohol to remove grease before ceramic deposition.

7.2.5. Electrophoretic deposition

The electrophoretic deposition cell (Fig. 7.1) was made of a pyrex container with nickel foam as the cathode, which was centered between two stainless steel 316 anode electrodes. The distance between cathode and anode was fixed at 1 cm. A constant voltage of 50 V was applied for EPD. The titania coated nickel foams were then sintered in 5 % hydrogen balance nitrogen at 900 ^{o}C with a heating and cooling rate of 1 °C/min. The microstructures of the deposited films were observed by using Hitachi S-2700 scanning electron microscope (SEM). The phase structures of materials were studied by using the Rigaku Rotaflex X-ray diffractometer (XRD) with Co Kα radiation.

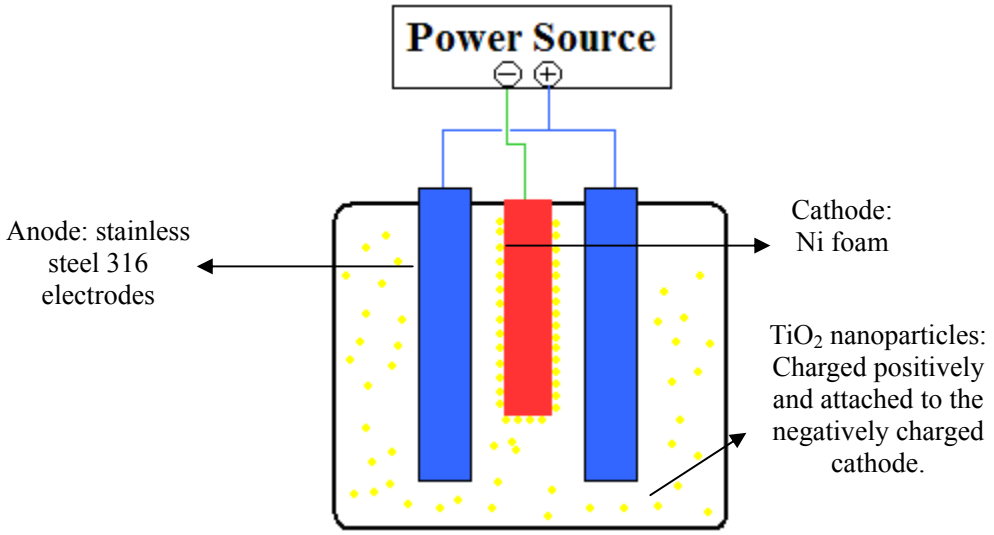

Figure 7.1. The schematic diagram for cathodic electrophoretic deposition setup.

7.3. Results and Discussion

7.3.1 Effect of triethanolamine (TEA) on the pH of the suspension

TEA used to stabilize titania in ethanol, butanol, and isopropanol [3, 15, 26]. The pH values of the titania suspension in ethanol and pure ethanol were measured as a function of TEA concentrations. Since the ethanol used in this experiment was dehydrated, pH measurement is not an accurate measuring method. However, these results did provide some information about the relationship between the ethanol, suspension and TEA concentrations. The pH value of pure ethanol was measured to be 6.25 but after the addition of titania, it decreased to 3.21 (Fig. 7.2). This confirmed the finding from others that the titania powder was acidic and it decreased the pH of the solution [26]. The TEA has a tertiary amine and a triol (i.e.a molecule with three alcohol groups) and it is a strong base due to the lone pair of electrons on the nitrogen atom. As a result, the addition of TEA into pure ethanol and the titania suspension increased the pH values of the solution. The pH values for both pure ethanol and the titania

suspension increased rapidly when TEA concentrations were increased from 0 to 0.5 g/L. The pH of pure ethanol and the titania suspension reached maximum values of 7.2 and 6.8, respectively at 1.3 g/L TEA concentration. Further addition of TEA did not increase their pH values.

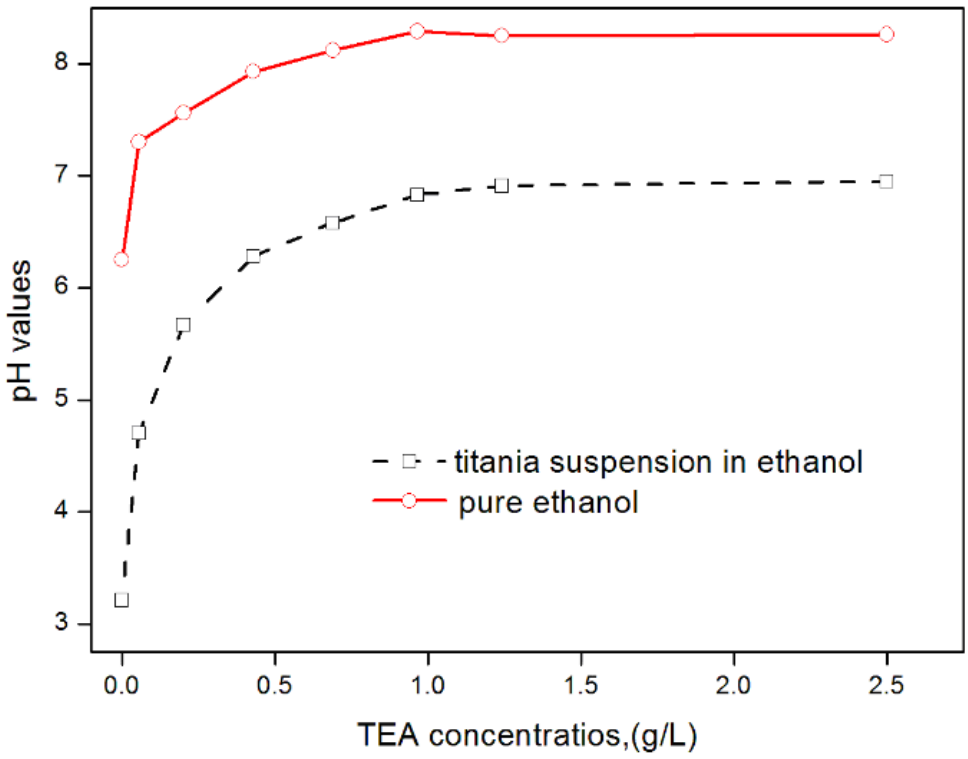

Figure 7.2. The pH of ethanol and titania suspension (2wt%) as a function of TEA concentration.

7.3.2. Effect of triethanolamine (TEA) on the conductivity of the suspension

Figure 7.3 shows the effect of TEA concentration on the conductivity of pure ethanol and titania suspension. Before adding TEA, the conductivity of pure ethanol and the titania suspension were measured to be 0.03 and 1.80 mS/cm, respectively. This indicated that the degree of ionization of TEA in ethanol was very low. The addition of TEA (0.05 g/L) into titania suspension increased the conductivity of suspension from 0.87 μS to 7.38 μS. As suggested [27], alcohols

can be self ionized into protonated alcohol (i.e. $CH_3CH_2OH_2^+$) and alkoxide ion (i.e. $CH_3CH_2O^-$) according to the following reaction:

$$CH_3CH_2OH + CH_3CH_2O\text{-}H \leftrightarrow CH_3CH_2O^- + CH_3CH_2OH_2^+ \qquad (7.1)$$

The protonated ethanol dissociates and leaves a proton on the particle surface and produces alcohol. As a result, the titania particles were positively charged in the alcoholic suspension due to the dissociated alcohol. Alcohols are known to be proton donors in the presence of bases. Consequently, the presence of TEA as a base can promote self ionization of ethanol. In addition, TEA can be dissociated on the particle surfaces and enhance the charging of particles in alcoholic based suspensions. The higher conductivity increase of the suspension when compared to conductivity variations of the pure ethanol when TEA added confirmed the effect of TEA on particle charging process.

The conductivity of the suspension significantly affects the electrophoretic deposition process and it is proportional to the ionic strength of the suspension [28]. The electrophoretic mobility (μ) of ceramic particles is a function of zeta potential (ζ), dielectric constant (ε), and medium viscosity (η) [29]:

$$\mu = \frac{\xi\varepsilon}{4\pi\eta} \qquad (7.2)$$

As shown in Equation (2), the electrophoretic mobility (μ) of ceramic particles greatly depends on the zeta potential since the dielectric constant (ε) became constant (ethanol is the suspension medium) and the medium's viscosity (η) can be neglected (the titania concentration in the suspension is very low). Therefore, the zeta potential is commonly used to measure the stability of the suspension for

EPD. When an electric field is applied, the ions in the suspension carry most of the current [30]. At high ionic concentration, the mobility of the particles is reduced due to the large amount of free ions in the suspension. In addition, at large ionic concentration, the rate of agglomeration increases forming large particles so that a uniform coating is difficult to obtain [28]. An optimum range of ionic concentration and suspension conductivity exists for the EPD process [31, 32]

The addition of TEA into the titania suspension had a remarkable effect on the suspension stability. Titania particle settle down and flocculates formed when TEA is not added to the suspension. The addition of TEA into the titania suspension improved its stability as was mentioned: The presence of TEA in ethanol increases the positive charge of the particles by leaving H^+ ions on their surface. [3, 26, 33]. Furthermore, the aliphatic chains of TEA may act as steric barriers between two particles and improve the dispersion particles stability [34].

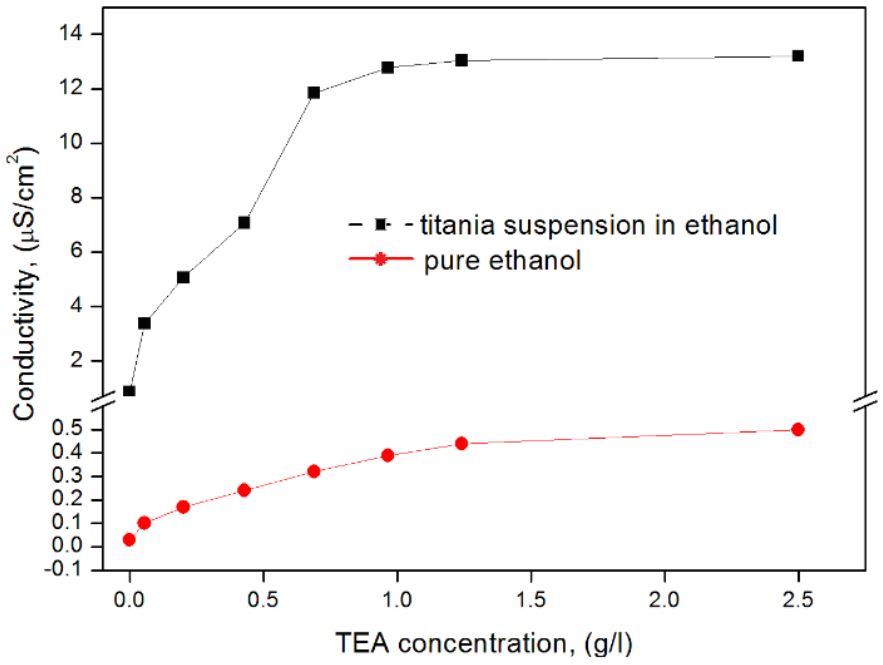

Figure 7.3. The effect of TEA concentrations on the conductivity of titania suspension and pure ethanol.

7.3.3. Electrophoretic mobility

The zeta potential and pH of the suspension containing 2 wt% titania in ethanol and TEA (0.2 g/L) were measured to be 7.12 and 7.5 mV, respectively. These results confirmed that the titania is positively charged at the pH value of 7. A stable titania suspension can also be obtained by carefully changing the operational pH. Figure 7.4 shows the dependence of zeta potential and conductivity of titania suspension on the operational pH of the suspension. The zeta potential for titania suspension was positive at low pH and became negative at high pH values. For a stable suspension, the zeta potential must locate from the isoelectric point (pH_{iep}) and the zeta potential can either be positive or negative. From the literature, the pH_{iep} (the pH value where the zeta potential of a suspension is zero) for titania suspension was measured to be between 5.5 and 7 [35-37]. The pH_{iep} in this experiment was found to be 7.8 and it was higher compared to the values obtained by others. The differences in the crystal structure of the titania powder might also alter the pH_{iep}. The titania powder used for this experiment was 100% anatase and others used a mixture of anatase and rutile. The effect of acid on the particles in non-aqueous media can be explained in three steps [27]: The nitric acid does not ionize in alcohols but adsorbs onto the basic sites of the particles in its undissociated form; The adsorbed acid molecules are dissociated by transferring hydrogen ions to the basic surface sites. During the adsorption-desorption process, some of the dissociated anions dissolved into

solution leaving positive charge on the particles. By adjusting the operational pH values of the suspension, the titania suspension with TEA has lower zeta potential compare to the titania suspension without TEA (Fig. 7.4). The addition of acid/base together with TEA decreased the stability of the titania suspension.

As shown in Figure 7.5, when the operational was pH increased from 7 to 11 or decreased from 7 to 1, the conductivity of the suspension increased. For an acidic suspension solution (pH 7-1), it reaches a maximum zeta potential and conductivity of 15.7 mV and 786 $\mu S/cm^2$, respectively. However, at the operational pH value of 1 (i.e.zeta potential of 15.7mV), the suspension was not stable. The conductivity of the solution affects the stability of the suspension as well as the deposition. If there are not enough ionic charges available they will not be sufficient force to move the particles. However, when the conductivity is increased, there are many others ions (i.e. NO_3^-, H^+) present in the suspension and this affects the stability of the solution. The suspension with pH values of 2.9 to 3.88 are stable and have high conductivity.

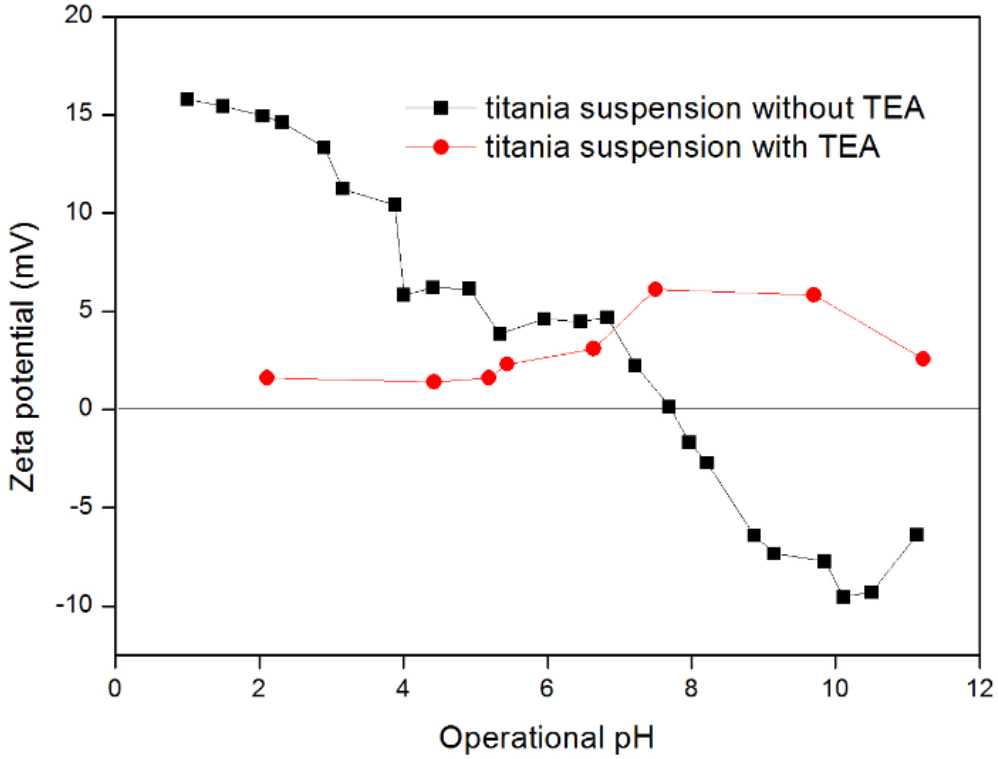

Figure 7.4. The zeta potential of titania suspension as a function of operational pH.

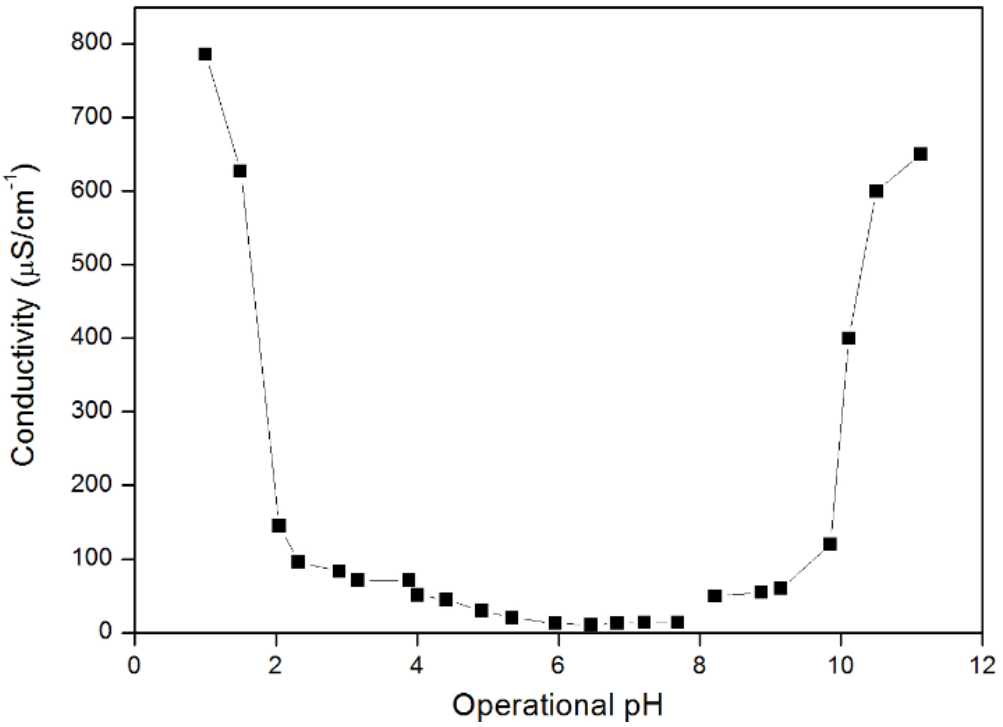

Figure 7.5. The conductivity of titania suspension as a function of operational pH. Acid (HNO_3) and base (NaOH) was used to adjust the operational pH.

Figure 7.6 shows the particle size distribution for a titania suspension with the addition of 2 wt% TEA and 15 minutes ultrasonication. The average particles size was determined to be 314 nm which was much larger than the particles size provided by the manufacturer (i.e. original size from manufacturer < 25 nm). In this experiment, ground and ultrasonication were also used in order to decrease average particles size of titania in suspension. The titania powder was ground at high speed of 300 rpm and grinding time was varied from five minutes to one hours. The ultrasonication was also conducted for different times which varied from five minutes to one hour. The grinding and ultrasonication did not have effect on decrease the average particle sizes.

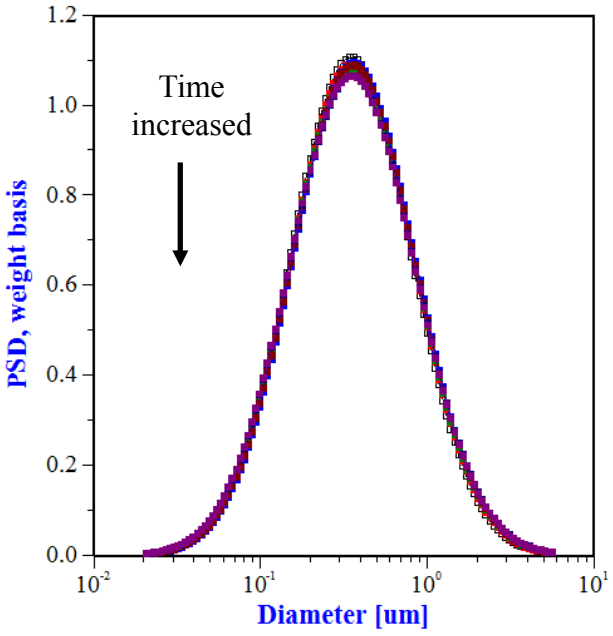

Figure 7.6. Particles size distribution for 2wt% titania suspension with additive of 2 wt% TEA.

7.3.4. The effects of triethanolamine (TEA) on deposition

The titania suspension without addition of TEA or adjusting operational pH exhibits the problem of rapid sedimentation. The suspension was unstable for a TEA concentration in the range 0 to 0.3 g/l. However, when TEA concentration was increased, the stability of the suspension also increased. The deposition rates were observed to be related to the concentration of TEA. No deposition was obtained for titania suspensions with TEA concentration in the range 0.1 to 0.5 g/l. The TEA affects the conductivity of the suspension. The conductivity for TEA concentration of 0.5 g/l was measured to be 8 $\mu S/cm^2$ (Fig. 7.2) and it was not sufficient for the movement of the particles. Ferrari and Moreno [38] studied the relationship between the electrophoretic deposition and conductivity of the suspension. When the suspension is too resistive, the particles are charged electronically and lose their stability; when the suspension is too conductive, particle motion is low. A large increased in the deposit weight was obtained when TEA concentration increased to 2 g/l. Above 2 g/l, the deposition rate becomes less sensitive to TEA concentration (Fig 7.6). As shown in Figure 7.2, the conductivity of the suspension became constant from 1 g/l onwards and the addition of TEA does not change the deposition rate. The zeta potentials remain constant with increasing of TEA concentration (Table 7.1). A TEA concentration of 2 g/l, yields good deposition rates.

Table 7.1. Effect of TEA concentration on the zeta potential.

TEA concentration (g/l)	Zeta pontential (mV)
0.5	7.17
1	7.11
2	7.12
3	7.26

7.3.5. The effects of PVB (polyvinyl butyral) on deposition

The polyvinyl butyral (PVB) is a common polymer binder additive in EPD processing, but the requirement of binder is usually minimal. The PVB acts as a binder which binds the deposits together and prevent cracks [32, 39, 40]. Furthermore, it can provide steric stabilization of the suspension for the ceramic particles [41]. According to the Extended-DLVO theory, the polymer layers can provide a repulsive potential known as steric stabilization which prevents the colloidal particles from combining with each other [42]. During electrophoretic deposition, both the ceramic and polymer particles deposit simultaneously on the electrode and the polymer can be included in the green body after solvent evaporation. The effect of PVB binder on the deposition rate is shown in Figure 7.7. The addition of 1 wt % PVB to the titania suspension containing 2 wt% TEA decreased the deposition rate. Increasing the amount of PVB would further lower the deposition rate. The decrease in deposition rate with the addition of PVB may be due to an increase in the viscosity of suspension. PVB increases the viscosity

of the suspension; a higher force is needed for the movement of the ceramic particles and thus decreases the deposition rate.

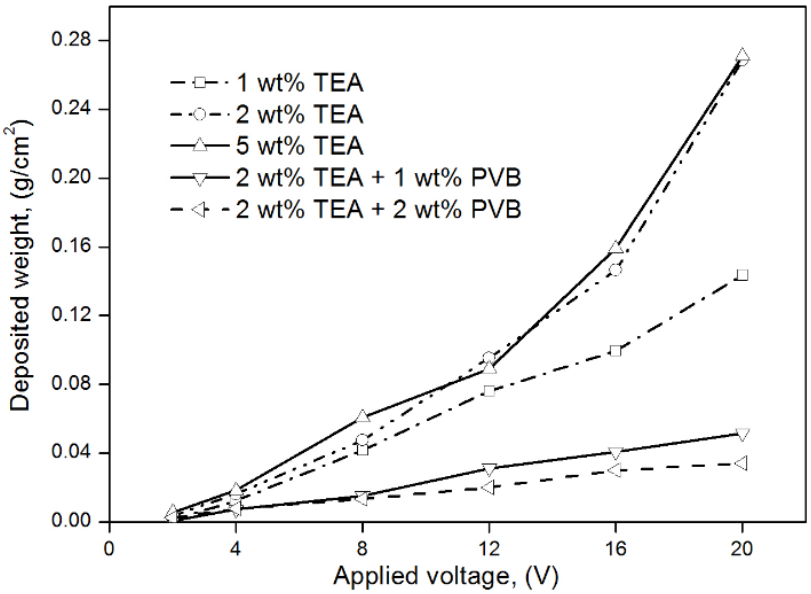

Figure 7.7. The deposition rate as a function of applied voltage with different additive to the suspension.

7.4 Using nickel foam as base substrate

Nickel foam was used as the base substrate for EPD. It has three dimensional (3-D) structure and the deposition becomes much more difficult when compared to 2-D structure (i.e. foil sample). One difficulty of deposition on 3D structures is the susceptibility to form hairline cracks during drying. In addition, coating the inside of the structure is another challenging problem that should be addressed. In our study, we found that stirring helps to improve the quality of the coating. The titania suspension was stired at high speed and titania could be coated in the inner part of the nickel foam. Figure 7.8 shows the SEM of the coating with different deposition times varied from 10 s to 30 s under a potential of 50 V. For 10 s of deposition time, the titania thickness is obviously thinner than for 20 s and 30 s.

The nickel foams were covered evenly by titania particles after 10 s deposition at 50 V. Hairline cracks were observed for the samples with 20 s and 30 s of deposition time after drying at room temperature. SEM images show that a uniform coating was deposited on the nickel foam after 10 s of deposition time. In addition, no cracks were detected after drying when compared to the other samples with higher deposition loadings. Since the nickel foam is a three dimensional structure, the drying rate for the deposited film was not uniform throughout. Some edges of the nickel foam dried faster and thus formed cracks. We observed that 10s is the optimum deposition time without development of cracks.

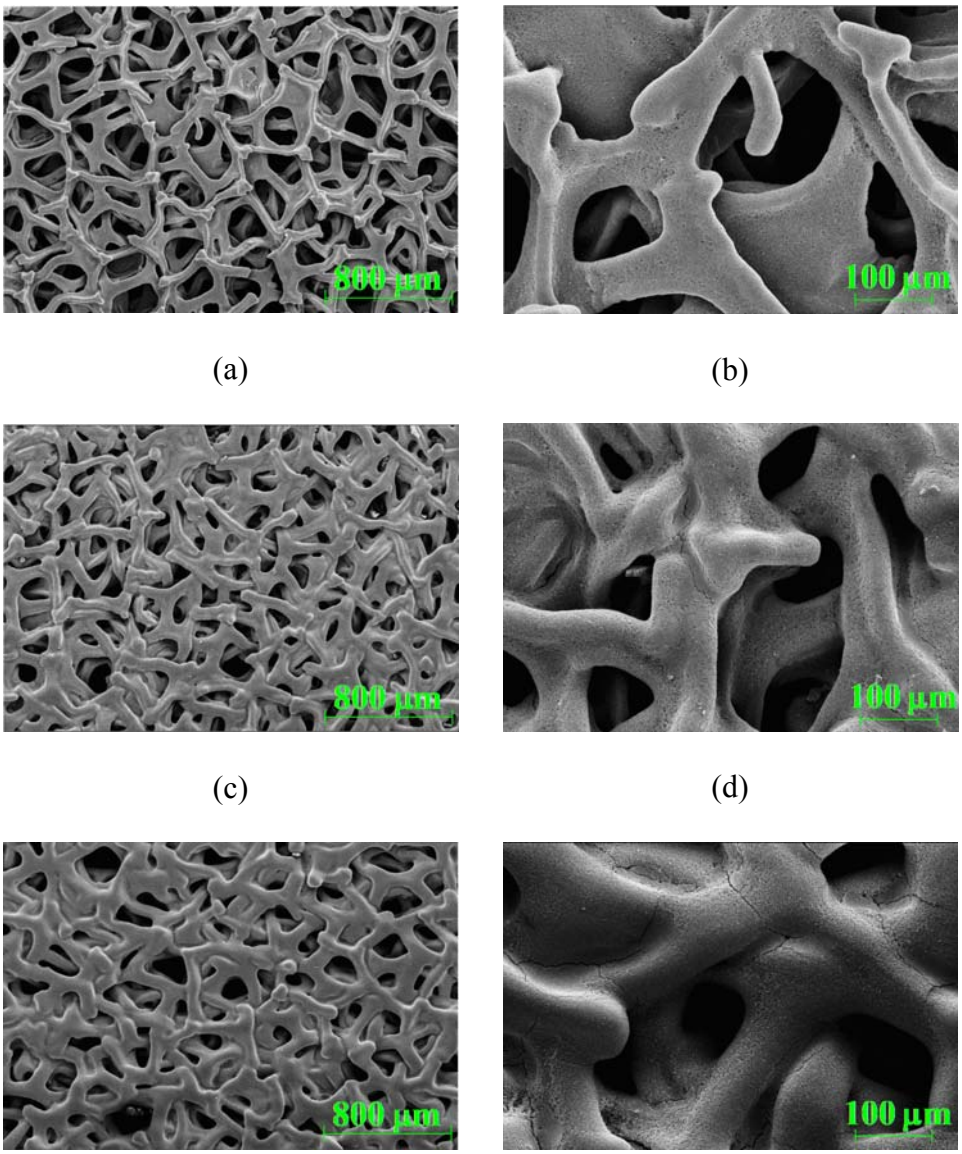

Figure 7.8. The titanium oxide coated nickel foam at potential of 50 V. (a) and (b) has deposition time of 10s; (c) and (d) has deposition time of 20s; (e) and (f) has deposition time of 30s.

Figure 7.9 shows the SEM images of titania coated nickel foam (10s deposition time) after heating in 5% hydrogen at 900^{o}C. During heating, the nickel foam did not change in dimension but the coating densifies and caused

shrinkage. Stresses were developed in the coating and released by the formation of cracks. The nickel foam has higher thermal expansion compared to titania coating. During heating, the nickel foam expanded faster than titania coating and caused cracks on the titania coating. The thermal expansion of nickel foam is not uniform at high temperature due to the 3-D structure. Anatase titania (TiO_2) was deposited on the nickel foam (Fig. 7.10). However, after reducing in H_2 at 900^{o}C, the coating formed Ti_5O_2 (Fig. 7.11). The change in phase for titania may also be responsible for crack formation. A smaller difference in thermal expansion coefficients between ceramic and metal can prevent cracks. The elimination of cracks during heating process will be the subject of future work for this project. The cracking formed during heating might be avoided by adding a liquid phase (i.e. glass enamel). In addition, a bond layer which has thermal expansion coefficient between the nickel foam and titania could be added to decrease the thermal expansion mismatch.

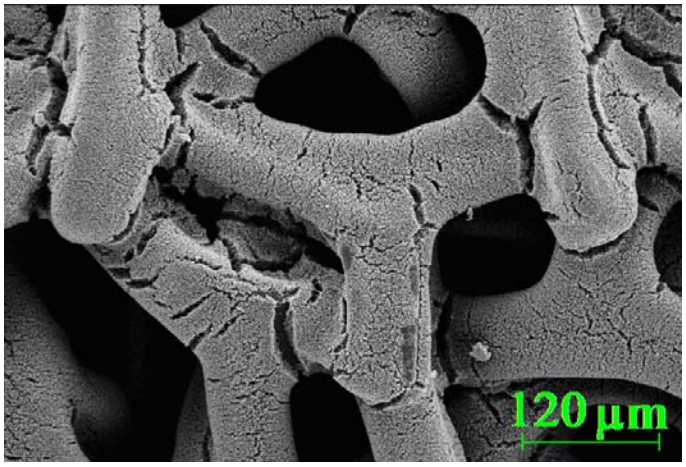

Figure 7.9. The SEM image of titanium coated nickel foam after heated in 5% hydrogen at 900^{o}C.

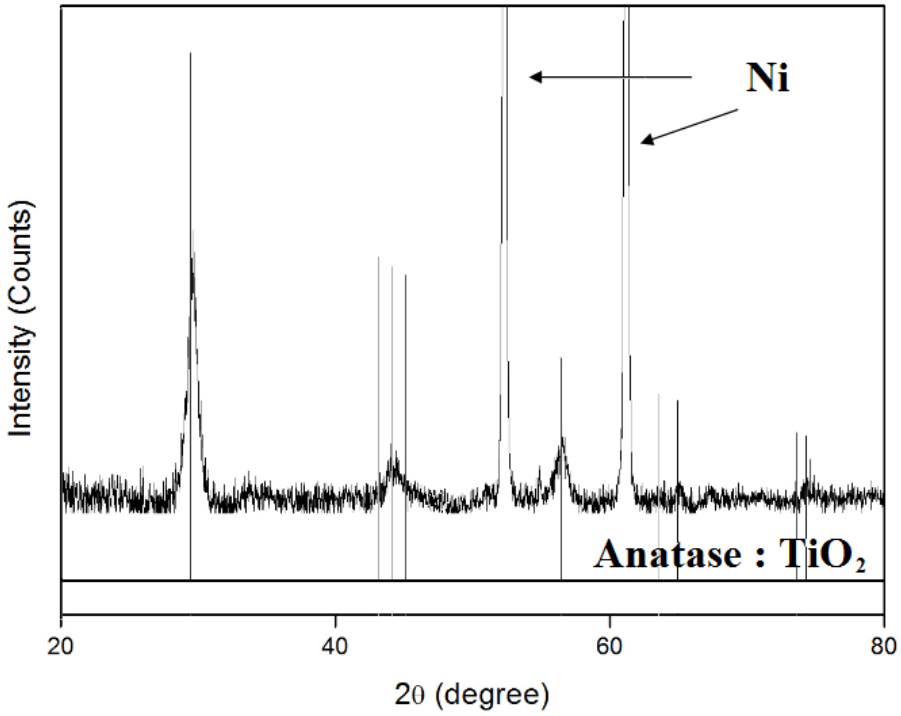

Figure 7.10. XRD pattern for titanium oxide coated nickel foam after 900°C heating in 5% hydrogen.

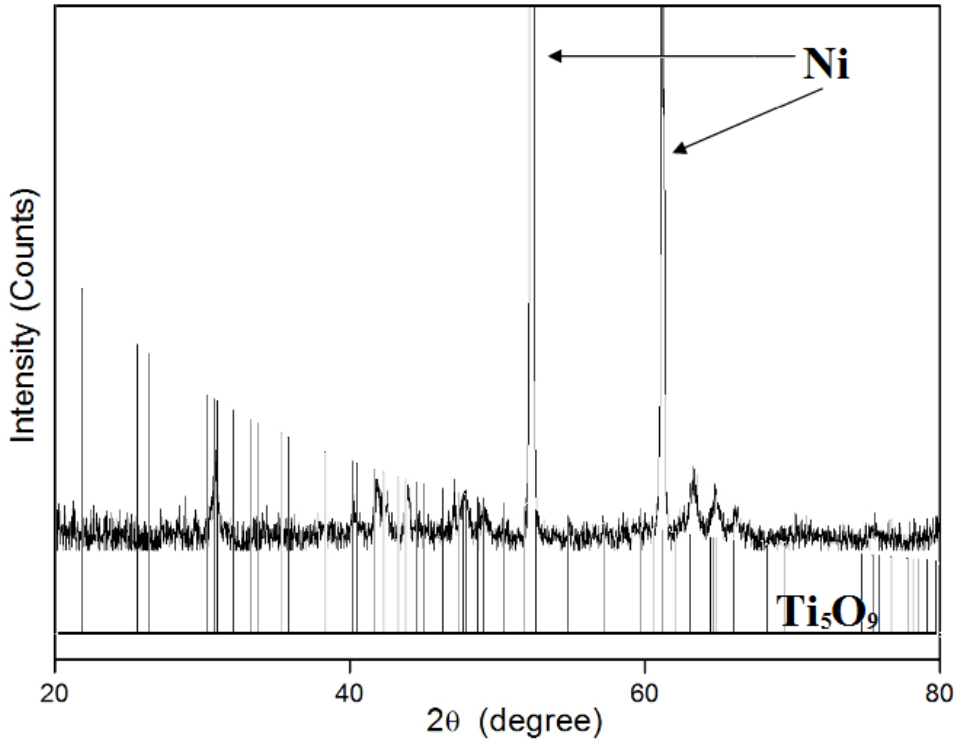

Figure 7.11. XRD pattern for titanium oxide coated nickel foam before heating.

7.5. Conclusions

The zeta potential of dilute (2wt%) titania in ethanol suspension was measured. A stable suspension was obtained by adjusting the pH of the suspension and by adding polyelectrolytes (i.e. TEA). The optimum suspension used for deposition contained 2 wt% titania, 2 wt% TEA and 1 wt% PVB. At applied voltage of 50V, and a deposition time of 10s , crack free deposit with high uniformity was coated on the nickel foam.

7.6. References

1. N. Wang, H. Lin, J. Li, X. Yang and B. Chi, *Thin Solid Films*, **496**, 649 (2006).

2. J. C. Yu, W. Ho, J. Lin, H. Yip and P. K. Wong, *Environmental Science & Technology*, **37**, 2296 (2003).

3. M. Ghorbani and M. Roushanafshar, *Key Engineering Materials*, **412**, 77 (2009).

4. A. R. Boccaccini, *Journal of Materials Science*, **41**, 8029 (2006).

5. K. Ellis, A. Hill, J. Hill, A. Loyns and T. Partington, *Journal of Power Sources*, **136**, 366 (2004).

6. A. H. P.C.S. Hayfield, *Int. J. Restorat. Build. Monuments*, **6**, 647.

7. S. R. Dhakate, V. K. Parashar, V. Raman and O. P. Bahl, *Journal of Materials Science Letters*, **19**, 699 (2000).

8. X. Gu, P. A. Trusty, E. G. Butler and C. B. Ponton, *Journal of the European Ceramic Society*, **20**, 675 (2000).

9. S. Kumaria, R. N. Singh and V. Gupta, *Journal of the American Ceramic*

Society, **79**, 199 (1996).

10. B. Meier, G. Grathwohl, M. Spallek and W. Pannhorst, *Journal of the European Ceramic Society*, **10**, 237 (1992).

11. R. Wurm, O. Dernovsek and P. Greil, *Journal of Materials Science*, **34**, 4031 (1999).

12. M. Santillán, F. Membrives, N. Quaranta and A. Boccaccini, *Journal of Nanoparticle Research*, **10**, 787 (2008).

13. O. O. Van der Biest and L. J. Vandeperre, *Annual Review of Materials Science*, **29**, 327 (1999).

14. P. Sarkar and P. S. Nicholson, *Journal of the American Ceramic Society*, **79**, 1987 (1996).

15. Shaohua Zhang, B. Xie and F. Li, *Key Engineering Materials* **336-338** 1953 (2007).

16. N. Koura, Y. Mikuriya and H. Shoji, *Hyomen*, **27**, 719 (1989).

17. I. Zhitomirsky, *Journal of the European Ceramic Society*, **18**, 849 (1998).

18. C. Kaya, F. Kaya, A. R. Boccaccini and K. K. Chawla, *Acta Materialia*, **49**, 1189 (2001).

19. O. van der Biest, S. Put, G. Anné and J. Vleugels, *Journal of Materials Science*, **39**, 779 (2004).

20. A. R. Boccaccini and I. Zhitomirsky, *Current Opinion in Solid State and Materials Science*, **6**, 251 (2002).

21. V. Paserin, S. Marcuson, J. Shu and D. Wilkinson, *Advanced Engineering Materials*, **6**, 454 (2004).

22. M. Ashby, T. Evans, N. A. Fleck, L. J. Gibson, J. W. Hutchinson and H. N. G. Wadley, *Metal Foams: A Design Guide*, p. 1, Elsevier Butterworth-Heinemann (2000).

23. J. Babjak, V. A. Ettel and V. Paserin, Method of forming nickel foam in *US Patent* C. Inco Limited (Toronto Editor, US (1990).

24. G. J. Davies and S. Zhen, *Journal of Materials Science*, **18**, 1899 (1983).

25. U. Köhler, C. Antonius and P. Bäuerlein, *Journal of Power Sources*, **127**, 45 (2004).

26. J. Widegren and L. Bergström, *Journal of the European Ceramic Society*, **20**, 659 (2000).

27. R. Damodaran and B. M. Moudgil, *Colloids and Surfaces A: Physicochemical and Engineering Aspects*, **80**, 191 (1993).

28. C. Wang, J. Ma, W. Cheng and R. Zhang, *Materials Letters*, **57**, 99 (2002).

29. J. H. Kennedy and A. Foissy, *Journal of the American Ceramic Society*, **60**, 33 (1977).

30. B. Ferrari and R. Moreno, *Materials Letters*, **28**, 353 (1996).

31. P. Sarkar, X. Huang and P. S. Nicholson, *Journal of the American Ceramic Society*, **76**, 1055 (1993).

32. F. Bouyer and A. Foissy, *Journal of the American Ceramic Society*, **82**, 2001 (1999).

33. X. F. Xiao and R. F. Liu, *Materials Letters*, **60**, 2627 (2006).

34. A. Das Sharma, A. Sen and H. S. Maiti, *Ceramics International*, **19**, 65 (1993).

35. D. E. Yates and T. W. Healy, *Journal of the Chemical Society, Faraday Transactions 1: Physical Chemistry in Condensed Phases*, **76**, 9 (1980).

36. G. R. Wiese and T. W. Healy, *Journal of Colloid and Interface Science*, **51**, 434 (1975).

37. G. A. Parks, *Chemical Reviews*, **65**, 177 (1965).

38. J. H. Kennedy and A. Foissy, *Journal of The Electrochemical Society*, **122**, 482 (1975).

39. J.-H. Jean, S.-F. Yeh and C.-J. Chen, *Journal of Materials Research*, **12**, 1062 (1997).

40. I. Zhitomirsky, *Journal of Materials Science Letters*, **17**, 2101 (1998).

41. L. Besra and M. Liu, *Progress in Materials Science*, **52**, 1 (2007).

42. F. Tepper, M. Lerner and D. Ginley, *American Ceramic Society Bulletin*, **80**, 57 (2001).

8.0 Conclusions and future work

8.1. Conclusions

Electrodeposition is an easy and effective method for forming protective coating on three-dimensional porous nickel foam. This technique is also industrially feasible and inexpensive since electrodeposition does not require complicated and costly deposition instruments. Copper coated nickel foam was fabricated by electrodeposition and exhibited strong resistance to carbon deposition and sulfur corrosion in carbon and/or sulfur containing gas at elevated temperature. In contrast, uncoated nickel foam suffered severe cracking and loss of mechanical strength after exposure to H_2S-containing syngas. The electrical resistance of copper coated nickel foam remained consistently low for 150 h in H_2S- containing syngas at 750^oC while that of uncoated nickel increased significantly. Based on the current work, copper coated nickel foam has significant potential value for use as current collector for solid oxide fuel cells fed by H_2S-containing syngas. Copper (i.e. copper foam) is not suitable to use individually as the current collector at high temperature application since it has melting point of 1083^oC. When coated nickel foam with copper, it formed copper-nickel alloy which has higher melting point (> 1200^oC).

A copper-ceria composite layer was co-electrodeposited on nickel foam and compared with copper coated nickel foam. The sulfur resistance abilities of these coatings were compared in H_2S-N_2 atmospheres. Both coatings showed increase in resistances and formed copper sulfide after exposure to H_2S-N_2. However, the copper-ceria composite layer showed better performance in H_2S atmosphere

compared to the copper coating. The ceria acted as a H_2S adsorbent and reduced the sulfidation rate of copper. Although the copper-ceria composite provided high sulfidation resistance, it cannot be used as protective coating for nickel foam due to crack formation.

A ceramic layer of TiO_2 was also coated on nickel foam using electrophoretic deposition. A stable TiO_2 suspension in ethanol was obtained by adding triethanolamine (TEA) and polyvinyl butyral (PVB). The isoelectric point was found to be pH 7.8. A crack-free coating was obtained after drying at room temperature. However, after heat treating the coated samples, cracks were formed. The differences in thermal expansion coefficient between the ceramic coating and metal foam were the reason for crack formation.

8.2. Future work

Theoretically, ceramic coating provides better stability in high concentration of H_2S when compared with to alloy coating. However, deposition of ceramic coating on nickel foam is a challenging process. The three-dimensional structure of nickel foam makes the deposition process even more difficult. It is difficult to cover the whole surface of nickel foam with dense ceramic layer. In addition, cracks may form on the ceramic coating when stress is applied. In further work, we will improve the process to coat the nickel foam with conductive and sulfur tolerant ceramic layer such as $La_{0.4}Sr_{0.6}TiO_3$ and test the properties as a current collector in the H_2S-containing syngas SOFCs.

Electrodeposition of metal on nickel foam is more suitable to prepare a conductive/protective coating on three-dimensional structure of nickel foam. In

future work, modification on the copper coating may be able to increase the stability for use in higher H_2S concentrations. Different deposition electrolyte solutions with additives can be investigated and the relationship between microstructure/ corrosion rate can be investigated. The microstructures of copper coating greatly affect the corrosion rate. In addition, the physical properties of the different copper coated nickel foams can also be examined.